SIMS bias on isotope ratios in Ca-Mg-Fe carbonates (Part III): $\delta^{18}O$ and $\delta^{13}C$ matrix effects along the magnesite-siderite solid-solution series

Maciej G. ŚLIWIŃSKI[1,3*], Kouki KITAJIMA[1,2,3], Michael J. SPICUZZA[1,3], Ian J. ORLAND[1,3], Akizumi ISHIDA[1,2,3,4], John H. FOURNELLE[3] and John W. VALLEY[1,2,3]

[1] *WiscSIMS, Department of Geoscience, University of Wisconsin-Madison, Madison, WI, 53706*
*Corresponding author: msliwinski@wisc.edu; +1 (425)-681-4288

[2]*NASA Astrobiology Institute, Department of Geoscience, University of Wisconsin-Madison, Madison, WI, 53706*

[3] *Department of Geoscience, University of Wisconsin-Madison, Madison, WI, 53706*

[4] *Department of Earth Science, Tohoku University, Sendai, Japan, 9808578*

Keywords: SIMS, carbon isotopes, oxygen isotopes, siderite, magnesite, matrix effects, carbonates

ABSTRACT

This study explores the effects of cation composition on mass bias (*i.e.,* the matrix effect), which is a major component of instrumental mass fractionation (IMF) in the microanalyses of $\delta^{13}C$ and $\delta^{18}O$ by SIMS in carbonates of the magnesite-siderite solid-solution series ($MgCO_3$-$FeCO_3$). A suite of 12 calibration reference materials (RMs) was developed and documented (calibrated range: Fe# = 0.002-0.997, where Fe# = molar Fe/[Mg+Fe]), along with empirical expressions for regressing calibration data (affording residuals <0.5‰ relative to CRM NIST-19).

The calibration curves of both isotope systems are non-linear and have, over a 2-year period, fallen into one of two distinct but largely self-consistent shape categories (data from 10 analytical sessions), despite adherence to well-established analytical protocols for carbonate $\delta^{13}C$ and $\delta^{18}O$ analyses at WiscSIMS (CAMECA IMS 1280). Mass bias was consistently most sensitive to changes in composition near the magnesite end-member (Fe# 0-0.2), deviating by up to 4.5‰ ($\delta^{13}C$) and 14‰ ($\delta^{18}O$) with increasing Fe-content.

The cause of variability in calibration curve shapes is not well understood at present, and demonstrates the importance of having available a sufficient number of well-characterized RMs so that potential complexities of curvature can be adequately delineated and accounted for on a session-by-session basis.

1. INTRODUCTION

Here we present the third installment of our on-going study of instrumental mass fractionation (IMF) and sample matrix effects (collectively referred to throughout as 'bias') in the analysis of carbon and oxygen isotope ratios from Ca-Mg-Fe carbonates by secondary ion mass spectrometry (SIMS). Building on early pioneering studies (*e.g.,* Eiler et al., 1997a; Valley et al., 1997; Fayek et al., 2001; Riciputi et al., 1998), we recently provided an empirical characterization of SIMS $\delta^{13}C$ and $\delta^{18}O$ bias for the dolomite-ankerite solid-solution series ($CaMg(CO_3)_2$-$CaFe(CO_3)_2$) and documented the development of a suite of micro-analytical reference materials (RMs) (Śliwiński et al., 2016a, 2016b). The focus here is on the basic

elements of the bias response from carbonate compositions that fall along the complete solid-solution that exists between the siderite ($FeCO_3$) and magnesite ($MgCO_3$) end-members of the Ca-Mg-Fe carbonate ternary (*e.g.,* Chai and Navrotsky, 1996; Chang et al., 1998). Carbonates of the siderite-magnesite series are encountered in many different geological environments; they occur, for example: 1) as siderite concretions in marine and fresh-water sediments (Curtis et al., 1972, 1986; Curtis, 1995; Gautier, 1982; Mozley, 1989a, 1989b; Postma, 1982); 2) as siderite nodules in wetland soils and sediments of the globe's humid climatic belts (Ludvigson et al., 2013, 1998; Sheldon and Tabor, 2009; Tabor and Myers, 2015; Ufnar et al., 2004); 3) as cements in sandstones and mudstones (Burley and Worden, 2003; Macquaker et al., 1997; Morad, 1998); 4) as ore-grade siderite and magnesite deposits (*e.g.,* Fernández-Nieto et al., 2003; Frost, 1982); 5) in the extensive banded iron-formations (BIFs) of the Precambrian (*e.g.,* James, 1954; Klein, 2005, see Figs. 1 and 2 therein); 6) in association with evaporitic sediments (*e.g.,* Bauluz et al., 1996; Botz and von der Borch, 1984; Lugli et al., 2001; Luzon et al., 2009; Mayayo et al., 1996; Mees and Keppens, 2013; Sanz-Montero and Rodríguez-Aranda, 2012); 7) in carbonatite complexes (*i.e.,* carbonate mineral-rich intrusive or extrusive igneous rock bodies; *e.g.,* Buckley and Woolley, 1990); 8) as inclusions in mantle diamonds (*e.g.,* Dobrzhinetskaya et al., 2001; Kaminsky et al., 2013; Sobolev et al., 1997; Wang et al., 1996); and 8) as a product of weathering or hydrothermal alteration of igneous and metamorphic rock bodies rich in Ca-Mg-Fe silicate minerals (*e.g.,* olivine, pyroxene, plagioclase, feldspars; *e.g.,* Chang et al., 1998 and references therein); such environments are being explored as one of many natural analogues to engineered CO_2 storage (*e.g.,* Power and Southam, 2005; Power et al., 2013; Wilson et al., 2009).

Carbonate compositions of the magnesites-siderite series are found in Martian meteorites (*e.g.,* Eiler et al., 2002; Niles et al., 2013), where they co-occur with members of the dolomite-ankerite series and other, more unusual compositions (from a terrestrial perspective) that are not constrained to either of these two solid-solutions. Similar compositions have been discovered in hydrothermally altered volcanic deposits in Spitzbergen (*e.g.,* Treiman et al., 2002) and are being explored as potential terrestrial analogues for understanding the formation of Martian carbonates (*e.g.,* Blake et al., 2010; Morris et al., 2011; Stern et al., 2013 and references therein).

The isotopic ratios of carbon and oxygen are widely used in the geosciences as proxies for inferring the conditions of carbonate formation; of interest most commonly is the temperature of mineral precipitation, the source(s) of carbon, and the nature/source of the fluids involved (*e.g.,* marine, meteoric, mixed or hydrothermal waters). Variations in the $\delta^{13}C$ and $\delta^{18}O$ signatures of pedogenic (soil) carbonates, for example, are frequently used as indicators of past ecologic and climatic change on the continents (Dworkin et al., 2005; Sheldon and Tabor, 2009; Suarez et al., 2010). As a further example, $\delta^{13}C$ and $\delta^{18}O$ records continue to be of interest for gaining insights into the diagenetic and metamorphic history of banded iron-formations (*e.g.,* Beukes et al., 1989; Beukes and Klein, 1990; Heimann et al., 2010; Kaufman et al., 1990b; Perry et al., 1973), as well as to make inferences about the unique paleoenvironmental conditions under which they formed, at least in so far as iron-formation carbonates constitute a suitable

proxy for the chemistry of ancient seawater and atmospheric CO_2 levels (see Heimann et al., 2010; Johnson et al., 2013). In many cases, however, the 'full-range' of isotope values within a sample (or some close approximation thereof) cannot be resolved and interpreted due to the technical limitations of the sampling methods employed in conventional isotope ratio mass spectrometry. This commonly involves generating sample powders by micro-drilling domains that are hundreds of micrometers in diameter (leading to potential signal averaging effects, especially in instances where multiple carbonate phases are present and crystal size is small).

The motivation for this research grew out of a need for RMs in the wake of recent technical advances in carbonate $\delta^{13}C$ and $\delta^{18}O$ microanalysis by SIMS, and the potential applicability of this technique to intensifying research efforts concerned with geologic carbon-sequestration (McGrail et al., 2016; Śliwiński et al., 2017). Isotope ratios in carbonates can now be routinely measured in-situ from micrometer-scale sample domains with sub-per mil (‰) repeatability (*sensu* VIM 2008, 2.20 and 2.21) (Valley and Kita, 2009). The accuracy of measurement (*sensu* VIM 2008, 2.13) in relation to a certified reference material (*e.g.,* NIST-19), however, depends in large-part on the availability and overall quality of matrix-matched RMs. That is, accuracy is limited by the extent to which RMs are chemically and isotopically homogenous on the spatial scale of intended use, and a sufficient number of these are needed to adequately characterize bias as a function of chemical composition (*e.g.,* Hervig et al., 1992; Valley and Kita, 2009). For many mineral families wherein the compositional end-members form extensive or complete solid-solutions with one-another – such as the carbonates - proper standardization remains a work in-progress for the community of SIMS laboratories around the world.

2. METHODS

The methodology employed is documented in detail in the first two parts of this study (Śliwiński et al., 2016a, 2016b). Thus, only a skeletal outline is provided here.

Clean grain splits (425-710 μm size-fraction) of 38 different naturally-occurring carbonate mineral specimens of the magnesite-siderite series (Table 1) were prepped after extracting approximately one-half to 1 cm^3 of the clearest or most visually-uniform domain of each sample. A suite of polished grain mounts was prepared and all 38 test materials were first evaluated for chemical zoning by BSE-SEM imaging (each grain mount contained twenty randomly-selected grains of five different specimens). The most visually uniform test materials (17 of the 38 in total) were then assessed by EPMA for variance in chemical composition (typically 3 spot analyses randomly placed on each of 20 grains) and later by SIMS to determine the extent of $\delta^{18}O$ and $\delta^{13}C$ uniformity (typically 1 spot on each of 20 grains). SIMS measurements were made using the CAMECA IMS 1280 large radius multicollector ion microprobe at the WiscSIMS Laboratory, Department of Geoscience, University of Wisconsin-Madison). Thirteen of these test materials (Table 1) were considered acceptable and lastly analyzed by conventional phosphoric acid digestion (12 hours, 100°C) and gas-source mass

spectrometry (McCrea, 1950) to calibrate the average $\delta^{13}C$ and $\delta^{18}O$ values relative to VPDB and VSMOW, respectively. In each case, a single 25-50 mg subsample of grains was powdered and three separate digestions were performed on ~5-mg splits. Phosphoric acid-fractionation factors for $\delta^{18}O$ measurements calculated based on composition using the formulation of Rosenbaum and Sheppard (1986).

Chemical homogeneity evaluations by EPMA were performed using either a 1-, 5- or 10-μm diameter beam (CAMECA SX-51 or SXFive FE, operated at 15 keV and 10-20 nA; see Supplementary Appendix 1 for RM-specific details). Fluorescent x-ray signals on all spectral peak positions (Mg, Ca, Mn and Fe Kα peaks, Sr-Lα) were measured for either 60 or 120 seconds. The guiding principle was to acquire at least 10,000 background-corrected Fe-Kα or Mg-Kα counts from the near end-member compositions that contain low concentrations of these elements (< 2 mol.%); this ensures that the relative standard deviation associated with x-ray counting statistics remains below 1%. Spectral background corrections were implemented using the Mean Atomic Number (MAN) method described by Donovan and Tingle (1996). During the course of a point analysis, the intensities of characteristic x-rays fluorescing from electron beam-sensitive materials can drift; this effect was monitored and corrected by a feature in Probe for EPMA software (Donovan et al. 2007) called 'TDI' (time-dependent intensity), where data plotted in *measured x-ray intensity* vs. *time* space are de-trended before ZAF corrections are applied.

3. A NOTE ON TERMINOLOGY AND DATA PRESENTATION

Measurements of carbon and oxygen isotope ratios in carbonate minerals by SIMS are affected by systematic inaccuracies arising from mass fractionation effects, a component of which is instrumental in nature. Fractionation occurs: 1) during secondary ion formation at the sample surface (sputtering); 2) during uptake and transmission through the mass spectrometer; and then again 3) during detection (*e.g.,* Eiler et al., 1997b; Fitzsimons et al., 2000; Hervig et al., 1992; Huberty et al., 2010; Valley and Kita, 2009). A further component of mass fractionation is related to sample composition, which varies systematically in minerals that exhibit solid-solution behavior (*i.e.,* the sample matrix effect) (*e.g.,* Eiler et al., 1997a,b; Ickert and Stern, 2013; Kitajima et al., 2015; Page et al., 2010; Riciputi et al., 1998; Śliwiński et al., 2016a, 2016b).

For a given SIMS configuration, these collective effects can be highly consistent across analytical sessions spread over a multi-year period (Śliwiński et al., 2016a, 2016b). Throughout this article, we will refer to the sum total of these effects as the $\delta^{18}O$ and $\delta^{13}C$ "bias." As defined by the International Vocabulary of Metrology (VIM, 2008), "measurement bias" is an "estimate of a systematic measurement error" (2.18, VIM 2008), the effects of which can be compensated for by a correction or calibration. A systematic measurement error, the causes of which can be known or unknown, is the "component of measurement error that in replicate measurements remains constant or varies in a predictable manner (2.17, VIM 2008)."

At present, secondary ion yields and the bias imparted to isotope ratios during sputtering cannot be accurately predicted from first principles for naturally-occurring minerals and glasses.

Further, the relative contributions of instrumental *vs.* sample matrix effects to the total measurement bias are unknown (see, however, the work of Fàbrega et al., 2017). Nonetheless, carbonate $\delta^{18}O$ and $\delta^{13}C$ values can be determined accurately by SIMS with proper standardization. Critically, bias can vary from session to session due to variations in instrumental parameters. For carbonate solid-solutions, this requires a sufficient number of well-characterized RMs to empirically characterize bias as a function of chemical composition on a session-by-session basis.

The bias associated with SIMS measurements of $\delta^{18}O$ and $\delta^{13}C$ values from RMs is expressed as follows:

$$\alpha^{18}O_{SIMS} = \frac{1+(\delta^{18}O_{raw}/1000)}{1+(\delta^{18}O_{VSMOW}/1000)} \quad \text{(Eq. 1)}$$

$$\alpha^{13}C_{SIMS} = \frac{1+(\delta^{13}C_{raw}/1000)}{1+(\delta^{13}C_{VPDB}/1000)} \quad \text{(Eq. 2)}$$

(modified after Kita et al., 2009). For each RM, the terms '$\delta^{18}O_{raw}$' and '$\delta^{13}C_{raw}$' represent the measured $^{18}O/^{16}O$ and $^{13}C/^{12}C$ ratios that have been corrected for background, drift, and detector dead-time (if electron multipliers are used) and respectively normalized to the $^{18}O/^{16}O$ ratio in Vienna Standard Mean Ocean ($^{18}O/^{16}O_{VSMOW}$ = 0.00200520 Baertschi, 1976) and the $^{13}C/^{12}C$ ratio in the Vienna Pee-Dee Belemnite ($^{13}C/^{12}C_{VPDB}$ = 0.0112372; Allison et al., 1995; Craig, 1957). They are thus expressed in the customary way as per mil deviations (‰; δ-notation) from the accepted values of the VSMOW and VPDB certified reference materials (CRMs). However, both terms are bias-uncorrected and are therefore not accurate relative to VSMOW and VPDB. The terms '$\delta^{18}O_{VSMOW}$' and '$\delta^{13}C_{VPDB}$,' on the other hand, represent the average $\delta^{18}O$ and $\delta^{13}C$ values of the same RM that have been independently calibrated to the VSMOW and VPDB scales by conventional phosphoric acid digestion and gas-source mass spectrometric analysis.

Values of $\alpha^{18}O_{SIMS}$ and $\alpha^{13}C_{SIMS}$ (eq. 1 and 2) are generally close to unity, and are therefore consistently expressed throughout this article using δ-notation and referred to as the '$\delta^{18}O$ bias' and '$\delta^{13}C$ bias,' respectively:

$$\text{bias (‰)} = 1000 \cdot (\alpha - 1) \quad \text{(Eq. 3)}$$

where α is either $\alpha^{18}O_{SIMS}$ or $\alpha^{13}C_{SIMS}$.

All equations presented here are formulated such that all mathematical operations involving multiplication or division are performed on α-terms, explicitly avoiding the common approximation where: $\delta_A - \delta_B \cong 1000\ln(\alpha_{A-B})$. Thus, for example, if two or more isotope ratios expressed using δ-notation are to be multiplied and/or divided, they are first converted to α-values, multiplied and/or divided, and finally converted back to isotope δ-values.

In order to construct working calibration curves that relate bias to chemical composition, the $\delta^{18}O$ and $\delta^{13}C$ bias of each RM was normalized (or "anchored") to that of end-member magnesite (UWMgs1):

$$\delta^{13}C \text{ or } \delta^{18}O \text{ bias}^{*}(RM - UWMgs1)(‰) = 1000 \cdot \left[\frac{1+(\text{bias}_{RM}/1000)}{1+(\text{bias}_{UWMgs1}/1000)} - 1\right] \quad \text{(Eq. 4)}$$

The '*' symbol indicates a normalized bias value. The associated propagation of analytical uncertainties are of the same general form as that reported in Śliwiński *et al.* (2016a; Supplemental Appendix S5).

In cross-plotting and examining $\delta^{13}C$ and $\delta^{18}O$ bias as a function of cation chemistry of the magnesite-siderite series, the composition is consistently expressed as the Fe/(Mg+Fe) molar ratio (*i.e.,* the Fe#).

Uncertainties associated with SIMS $\delta^{13}C$ and $\delta^{18}O$ measurements are reported in one of two ways:

1) As a standard deviation value (at the 95% confidence level) for a sample of a population ($2s = 2\sqrt{\frac{\Sigma(x-\bar{x})^2}{(n-1)}}$, where $\bar{x}$ is the average (statistical mean) of a set of n values). This is relevant in reporting: 1) the level of isotopic homogeneity of each evaluated RM (where the intent is to show the extent to which individual measurements are spread about the mean), and 2) the measurement precision for a single sample spot-analysis (based on the $2s$ value of 8 repeat measurements of a drift-monitoring material that brackets each set of ~10 sample measurements).

2) As a standard error of the mean (at the 95% confidence level) for a sample of a population ($2se = 2s/\sqrt{n}$, where n is the number of observations). This is particularly relevant to calibration diagrams, where the $2se$ value reflects upon how well the average is known for each set of replicate RM measurements. As the number of replicate measurements (n) increases, the average value calculated for each RM becomes a more reliable estimate of each respective population average. Uncertainties associated with regression parameters are also expressed as $2se$ values.

A useful review of the uncertainties associated with SIMS measurements can be found, for example, in Fitzsimons et al. (2000).

4. Results and Discussion

4.1. Summary of chemical homogeneity assessments

The calibration suite consists of 12 reference materials (see Table 1). The complete solid-solution that exists between the magnesite ($MgCO_3$) and siderite ($FeCO_3$) end-members is uniformly represented by 11 different carbonate compositions (Fe# 0.002 to 0.997; see Table 2). Note that two of the materials sourced from different localities (UWMgs4 and 5a,b) share a similar cation chemistry but are isotopically dissimilar (making for 12 RMs in total). Variability

in the molar Fe/(Mg+Fe) ratio (*i.e.,* Fe#) is as small as 0.001 (2*s*) and does not exceed 0.022 (2*s*) Fe# units. For most RMs in the suite, the relative standard measurement uncertainty ($100 \times 2s/average$; 95% confidence level) falls between 0.1 and 13.7%. The relatively high value (33.6%) associated with UWMgs2 – which contains 1.25% $FeCO_3$ – reflects greater chemical heterogeneity compared to all other RMs in the suite, requiring a larger number of replicate analyses for routine use (typically at least 8). In the case of the magnesite end-member (UWMgs1), however, the high relative standard measurement uncertainty value (49%) is associated with only a trace concentration of Fe (0.17% $FeCO_3$), which has no measurable effect on $\delta^{18}O$ or $\delta^{13}C$ bias.

Less than 1% $MnCO_3$ is present in RM compositions near the magnesite end-member (Fe# < 0.15), whereas all others generally contain <5% (the one exception is UWSd4, with 8.35%). The entire suite contains up to ~1% $CaCO_3$ and no detectable Sr (detection limit of 0.001% $SrCO_3$).

The complete EPMA dataset is provided as a Supplementary Appendix (1).

4.2. Summary of isotopic homogeneity assessments

The level of isotopic homogeneity of each RM on the microanalytical scale was assessed using a 10-µm diameter spot-size for $\delta^{18}O$ and a 6-µm spot-size for $\delta^{13}C$ measurements. Typically, ~20 different grains were analyzed once each.

Of the 12 RMs in total, 8 yielded $\delta^{18}O$ datasets with 2*s* < 0.56‰ (2*s*; see Table 1). An additional 3 RMs yielded 2*s* values within ±0.86‰, and are considered to be routinely usable for calibration if the 2*se* value is driven to ≈0.3‰ with a sufficient number of replicate measurements (approximately 8 measurements are required in this case from a handful of grains, whereas more uniform RMs require as little as four). For reference consider that a 2*s* value of 0.3‰ is expected for $n = 4$ replicate measurements performed on a nominally homogenous material; this is based on considerations of ion counting statistics, overall instrument stability and slight mount-specific differences in $\delta^{18}O$ bias values measured from drift-monitoring materials (*e.g.* Kita et al., 2009; Valley and Kita, 2009). In the case of RMs with slight heterogeneity, a 2*s* value of up to approximately ±0.5‰ is considered acceptable. Reference material UWMgs7 is not preferred for routine use on account of a 2*s* value of 1.89‰ and the large number of replicate measurements (20+) required to drive the 2*se* value to 0.4‰. However, data for this material is being presented because it nonetheless provides critical insight into the magnitude of SIMS $\delta^{18}O$ bias in the compositional range between Fe# 0.2 to 0.4, for which it was difficult to obtain samples in sufficient quantity for RM development.

All 12 RMs yielded $\delta^{13}C$ datasets with 2*s* values <1.0‰ (2*s;* Table 1). Based on the same considerations as above, a 2*s* value of 0.6-1.2‰ is expected for $n = 4$ replicate measurements using the instrumental configuration and analytical protocol employed at WiscSIMS for small-spot carbonate $\delta^{13}C$ analyses (6-µm diameter spot-size). Please note that in comparison to oxygen, measurements of carbon isotope ratios are inherently more variable because: 1) carbon has a lower ionization efficiency than oxygen under comparable primary ion beam conditions,

and 2) carbon comprises only 20% of all atoms in the carbonate crystal structure (compared to oxygen which accounts for 60%), requiring the use of an electron multiplier for detecting the secondary $^{13}C^-$ ion stream.

Replicate $\delta^{18}O$ and $\delta^{13}C$ measurements of mg-sized grain-splits of each RM by phosphoric acid digestion and gas-source mass spectrometry yielded 2*s* values no larger than 0.14‰ and 0.04‰, respectively (Appendix A). The range of $\delta^{18}O$ values represented by the entire suite extends from 7.92 to 16.99‰ VSMOW (-22.30 to -13.50‰ VPDB), whereas the $\delta^{13}C$ range extends from -11.97 to -0.32‰ VPDB.

The complete SIMS dataset is provided as a Supplementary Appendix (2).

4.3. Calibrations (overview)

In the first two parts of this study, we empirically constrained the behavior of SIMS $\delta^{18}O$ and $\delta^{13}C$ bias for carbonate mineral compositions of the dolomite-ankerite solid-solution series and introduced the use of a Hill-type equation (Goutelle et al., 2008; Hill, 1910) as an adequate means of mathematically modeling the highly non-linear distribution of calibration data in composition *vs.* bias space (equation 4 in Śliwiński et al., 2016a, 2016b):

$$\delta^{18}O \text{ or } \delta^{13}C \text{ bias}^*(RM - RM_{end-member\ dolomite}) = \frac{(Bias^*_{max})\, x^n}{k^n + x^n} \quad \text{(Eq. 5)}$$

where *'x'* = Fe#, *'k'* and *'n'* are curve-shape parameters and *'Bias*$_{max}$'* is an analytical session-specific scaling factor. Note that the bias of each RM is normalized to that of an end-member dolomite ('UW6220' at WiscSIMS), which serves as the 'anchor' for the dolomite-ankerite series (the asterisk denotes that bias values have been normalized to the calibration anchor). Under routine operating conditions for carbonate $\delta^{18}O$ and $\delta^{13}C$ analysis at WiscSIMS, this equation has been reliably applied over a 3-year period using the same set of curve-shape parameter values to regress calibration data acquired using: 1) 10-µm spot-size $\delta^{18}O$ analysis conditions; 2) 3-µm spot-size $\delta^{18}O$ conditions; and 3) 6-µm spot-size $\delta^{13}C$ conditions (additional calibration datasets have been acquired since publication of Parts I and II of this study (*e.g.,* Brodie 2016, Haroldson, 2017), but no significant changes in the values of the curve-shape parameters have been observed).

Unlike the dolomite-ankerite bias calibrations, the magnesite-siderite trends have unexpectedly behaved less consistently from session to session, and have shown more complexity of curvature. Throughout the two-year time span of RM development, we have acquired calibration data for the magnesite-siderite series on multiple occasions; the dataset presented here includes measurements from: 1) four separate 10-µm spot-size $\delta^{18}O$ sessions; 2) two 3-µm $\delta^{18}O$ sessions; and 3) four 6-µm $\delta^{13}C$ sessions (see data summaries in Tables 3 and 4). The behavior of $\delta^{18}O$ bias calibrations fell into one of two categories: the first consists of trends with two inflection points at constant positions along the compositional axis ("Type-I" calibrations; data from three 10-µm spot-size sessions and one 3-µm session) and the second of trends with only one inflection point (Type-II; data from one 10-µm spot-size session and one 3-

μm session). The behavior of $\delta^{13}C$ bias calibrations also fell into one of two categories of trends with no inflection points: those resembling the general shape of a 3rd-order polynomial (Type-I), and those that could be adequately regressed using a 2nd-order polynomial (Type-II). Two of four sessions represent each type of $\delta^{13}C$ bias calibration.

Shown in the main body of this work are $\delta^{18}O$- and $\delta^{13}C$-bias calibrations constructed using measurements from a single mount containing the full suite of RMs (data from sessions: S23 (6-μm $\delta^{13}C$), S22 (10-μm $\delta^{18}O$) and two 3-μm $\delta^{18}O$ sessions - S24 and S26). Shown also, including in Supplemental Appendix 3, are additional examples of calibrations from earlier (intermediate) stages of development during which time the suite of RMs was distributed among multiple grain mounts (each containing up to 20 grains of 5 different test materials; see Table SA 3-1 for details). These additional examples are included here to demonstrate that the two $\delta^{18}O$ bias trend types we discuss have been reproducible. Any mount-specific differences in bias measured from any one RM are expected to be < 0.5‰ (2*s*). Consider, for example, the dataset from session S19 (Supplementary Appendix 2), where four different mounts were used in building the magnesite-siderite calibration. For any one mount, the average $\delta^{18}O$ bias value of the co-mounted drift-monitoring material (calcite "UWC-3"; Kozdon et al., 2009) differs by < 0.5‰ relative to all other mounts. Thus, any potential mount-to-mount bias differences do not provide a tenable explanation for the existence (at present) of two different $\delta^{18}O$ and $\delta^{13}C$ trend types. Note in particular that both types of $\delta^{18}O$ bias behavior have been observed on separate occasions using the same set of grains on a single calibration mount using the same 3-μm spot-size $\delta^{18}O$ configuration (Table SA 3-1).

4.3.1. THE BEHAVIOR OF SIMS $\delta^{18}O$ BIAS ALONG THE MAGNESITE-SIDERITE BINARY

In all instances (Type-I and II trends), the change in the $\delta^{18}O$ bias (un-normalized) between the end-members of the magnesite-siderite solid-solution series was not unidirectional. To a first-order, however, the magnitude of the bias *decreased* as a function of increasing Fe-content (Fig. 2a-b). In other words, the per mil difference between $\delta^{18}O_{raw}$ as measured by SIMS and the 'accepted' $\delta^{18}O_{VSMOW}$ values became *smaller*. The bias was always largest for end-member magnesite (approximately -20 to -25‰ with 10-μm spot-size and -35‰ with 3-μm spot) and different by 12-16‰ in relation to end-member siderite (approximately -8 to -12‰ with 10-μm spot and -20‰ with 3-μm spot). From here on the discussion will focus on *working calibration curves* (Fig. 2c-d), for which $\delta^{18}O$ bias values were normalized to the RM with Fe# = 0 (*i.e.,* values expressed as $\delta^{18}O$ bias*(RM-UWMgs1)), and thus are seen to increase with Fe#.

4.3.1.1. TYPE-I $\delta^{18}O$ TRENDS

10-μm spot-size setup (3 sessions): The more common Type-I $\delta^{18}O$ calibrations can be described as follows. A representative trend is shown in Figure 2c (session S22 data). The magnitude of SIMS $\delta^{18}O$ bias*(RM-UWMgs1) increased exponentially by ~13.5‰ between Fe# = 0.0 and the first inflection point at Fe# = 0.25. This was followed by a gradual decrease of ~4‰ out to the second inflection point at Fe# = 0.70, and lastly an upward rebound of ~2.5‰

between Fe# = 0.7 and 1.0. The calibration data were regressed using the following mathematical expression, which stems from the probabilistic properties of the same Hill function (*e.g.,* Goutelle et al., 2008; Hill, 1910) used in recent work on $\delta^{18}O$ and $\delta^{13}C$ matrix effects in the dolomite-ankerite series (Śliwiński et al., 2016a, 2016b). Hill-type equations are well-suited for describing empirical relationships between the intensity of a measured effect (or response) and the concentration of a certain component(s) in the system under observation, especially in the case of systems that behave nonlinearly and reach saturation:

$$\text{bias}^*(\text{RM} - \text{UWMgs1}) = C_1\left(\frac{nx^{n-1}}{k^n + x^n}\right) + C_2x^d + C_3 \qquad \text{(Eq. 6)}$$

With the addition of the 'x^d' term along with the three constants 'C_1', 'C_2', and 'C_3', this is a modified form of equation 27 of Goutelle et al. (2008), where 'n', 'k' and 'd' are curve shape parameters and 'x' in our application is the Fe# of either a sample or RM. The influence of the shape parameters on the regression is shown graphically in Figure SA 3-1, along with a step-by-step graphical description of the trend-fitting process. The constants 'C_1' and 'C_2' allow for vertical stretching/compression of the working calibration curve (Fig. 2c, session S22 trend) to account for the fact that measured bias values can differ by up to several ‰ on a session-to-session basis (a new session is defined any time significant changes are made in tuning parameters; typically a session lasts from two to five days). Lastly, the constant 'C_3' accounts for the fact that the calibration curves would not be anchored to the origin (0,0) if an RM other than UWMgs1 were used as the normalizer (thus in the present case 'C_3' = 0). This becomes relevant when one attempts to fit a surface model to bias data for the entire Ca-Mg-Fe carbonate ternary. For this, it is necessary to normalize the bias of all carbonate RMs (*i.e.,* calcites, dolomite-ankerites, magnesite-siderites) to a common 'anchor.' Consider, for example, setting dolomite rather than magnesite as the common normalizer (*i.e.,* the (0,0) point). Doing so would have the effect of offsetting the regression of the magnesite-siderite series by the magnitude of the bias difference between the two RMs (*i.e.,* $\delta^{18}O$ bias*(dolomite$_{\text{end-member}}$ − magnesite$_{\text{end-member}}$)), but would have no effect on the overall shape of the calibration curve. Because 'C_3' is simply a ratio of two measured values, it does not need to be determined by a fitting algorithm, leaving equation (6) an empirical expression of five-parameters.

Regressing the oxygen isotope bias data from the full suite of calibration RMs (Figure 2c, session S22) yields the following curve shape parameter (n,k,d) and constant (C_1, C_2) values (± 2*se*): n = 1.8 (± 0.1), k = 0.26 (± 0.04), d = 4.2 (± 2.9), C_1 = 3.8 (± 1.0) and C_2 = 5.9 (± 1.2), and C_3 = 0. This same set of curve shape parameter values was successfully applied in regressing calibration data from two earlier sessions during which fewer RMs were available (Fig. SA 3-2). In all three instances, the measured average value of $\delta^{18}O$ bias*(RM-UWMgs1) for all RMs differs by less than 0.5‰ from the output of the calibration model (see residual plots in Figs. 2c and SA 3-2). This can be considered a measure of accuracy in relation to CRM NIST-19 (Verkouteren and Klinedinst, 2004). The calibration residual shows no significant correlation to the minor Ca-content of some of these materials (r = 0.04; up to 1.07 mol% $CaCO_3$ end-

member), nor to the more substantial Mn concentrations (r = 0.19; up to 8.35 mol% $MnCO_3$ end-member). No secondary matrix corrections were thus required for this particular suite of RMs.

Including Mn in the Fe# calculation, on account of its appreciable concentration in the RM suite and the overall similarity of Mn^{2+} to Fe^{2+} in terms of mass and ionic radius, neither significantly improved nor degraded the quality of the regression (see Fig. SA 3-3). Note, however, that the most Mn-enriched RMs in the suite do not fall near the magnesite end-member of the solid-solution series, where $\delta^{18}O$ bias changes most rapidly as a function of cation chemistry. It is likely for this reason that the regression remains unaffected. In the hypothetical case of samples that are enriched in Mn but deficient in Fe, it may be advisable to plot bias as a function of (Fe+Mn)# (*i.e.,* molar (Fe+Mn)/(Mg+Fe+Mn)), although future studies will need to resolve more conclusively how the effects of Mn-substitution on $\delta^{18}O$ bias in both the magnesite-siderite and dolomite-ankerite series compare to those of iron.

3-µm spot-size setup (1 session): A different set of routine analytical conditions is used at WiscSIMS for 3- *vs.* 10-µm spot carbonate $\delta^{18}O$ analyses (described in Śliwiński et al., 2016a). Notably, the small 3-µm spot-size configuration makes use of a weaker primary Cs^+ ion beam (600 pA vs 1.2 nA) and employs an electron-multiplier for detecting the minor isotope ($^{18}O^-$) in the secondary ion stream (as opposed to a Faraday cup). One of the two 3-µm calibrations generated to date strongly resembled the three self-consistent 10-µm trends (Fig. 2d, session S26 data; compare to session S22 trend in Fig. 2c) and was successfully modeled using the same empirical expression (eq. 6), yielding residuals ≤ 0.5‰ (Fig. 2d) and the following parameter values (± 2*se*): n = 1.9 (± 0.1), k = 0.24 (± 0.06), d = 1.6 (± 1.9), C_1 = 3.9 (± 1.8) and C_2 = 5.8 (± 2.4), and C_3 = 0. Note that the values of the curve-shape parameters n and k and the constants C_1 and C_2 are within 2*se* limits of those associated with the 10-µm trends.

This 3-µm trend differs from the above-mentioned 10-µm calibrations in that the magnitude of SIMS $\delta^{18}O$ bias*(RM-UWMgs1) increased markedly by ~15.5‰ (*i.e.,* by an additional 2‰ compared to the 10-µm trends) between Fe# = 0.0 and the first inflection point at Fe# = 0.25. At the present time, however, this should not be viewed as a general conclusion about differences between 3- and 10-µm calibrations. The number of datasets is still limited, and this 2‰ difference in the magnitude of the maximum bias between the end-members of a solid-solution falls within the general range of expected session-to-session variability (compare with Śliwiński et al., 2016a, 2016b). A potentially more meaningful difference may lie in the observation that the bias maximum (relative to UWMgs1) at Fe# = 0.25 is followed by a more gradual decrease of ~3‰ out to the second inflection point at Fe# = 0.7 and the disappearance of a significant rebound between Fe# = 0.7 and 1.0 (compared to 10-µm trends).

4.3.1.2. TYPE-II $\delta^{18}O$ TRENDS

10-µm and 3-µm spot-size setups: The alternate behavior of $\delta^{18}O$ bias calibrations, shown in Figure 2c-d, has been observed under both 10- and 3-µm spot-size conditions. These Type-II trends represent two of the six sessions to date. The behavior can be described as follows. Starting at Fe# = 0.0, the magnitude of SIMS $\delta^{18}O$ bias*(RM-UWMgs1) in both

instances increases exponentially and reaches a maximum of ~16.5‰ around Fe# = 0.4-0.5. Values then steadily decline by 1-2‰ out to Fe# = 1.0. This behavior was modeled by combining the Hill equation (in the form used to model bias in the dolomite-ankerite series; Eq. 5 herein) and the second term of Eq. 6, which allows the Hill function to descend after reaching a maximum value:

$$\text{bias}^{*}(\text{RM} - \text{UWMgs1}) = \left(\frac{Bias^{*}_{max}\, x^{n}}{k^{n}+x^{n}}\right) + C_{2}x^{d} \qquad \text{(Eq. 7)}$$

All terms are as defined earlier.

4.3.2. ASSESSMENT OF POTENTIAL CRYSTALLOGRAPHIC ORIENTATION EFFECTS ON $\delta^{18}O$ BIAS

To our knowledge, crystallographic orientation effects on $\delta^{18}O$ bias (analogous to those described by Huberty et al., 2010; Kita et al., 2011) have not yet been investigated for carbonates of the magnesite-siderite series. We performed a simple test using two different mounts, each containing grains of siderite (RM UWSd1) and two ferroan-magnesites (RMs UWMgs4 and 5a) exposed at the analytical surface in one of two broadly different sets of orientations with respect to the primary and secondary ion beams.

The first category of orientations includes those where the rhombic cleavage of magnesite and siderite grains is parallel to sub-parallel with regards to the flattened and polished analytical surface of the 1-inch diameter epoxy mount; these orientations tend to be over-represented when laying out grains on casting plates, although the variable rotational positioning of cleavage faces does diversify the number of unique crystallographic orientations that will eventually be exposed for measurement. It does not, however, allow for an assessment of whether $\delta^{18}O$ bias differs significantly along the crystallographic planes that are normal to sub-normal to: 1) rhomb edges or to the 2) rhomb body-diagonal long axis. These orientations comprise the second category. A grain mount was prepared with only this second category of orientations exposed by supporting grains during casting with strips of ridged carbon tape arranged in a series of parallel trenches ~0.5 mm deep and spaced ~0.5 mm apart (Fig. SA 3-4).

Measurements of $\delta^{18}O$ bias from both mounts were performed on the same day of analysis (session S21) and were found to be well within the ±0.3‰ *2s* repeatability of the UWC-3 bracketing RM used to monitor instrument drift (Table 5). In other words, there is no significant difference in bias between the two broad categories of crystallographic orientations described above.

4.3.3. CURRENT INSIGHTS AND FUTURE DIRECTIONS TOWARDS UNDERSTANDING THE COMPLEXITIES OF $\delta^{18}O$ BIAS TRENDS FOR THE MAGNESITE-SIDERITE SERIES

The $\delta^{18}O$ bias response of carbonate compositions between Fe# 0 and 0.3 is comparable for Type-I and -II calibrations under both 3- and 10-µm spot-size conditions (Fig. 2c and d; for ease of comparison, all four trends are co-plotted in Fig. SA 3-5). Recall that calibration trends can stretch or contract by up to several per mil along the bias axis from session to session while

maintaining constant curve-shape parameter values (and that a session-specific scaling factor relates them; Śliwiński et al., 2016a,b). Divergence in trend shape is driven by the session-specific trajectory taken by compositions beyond Fe# 0.5, and has, to date, resulted in bias differences of 2-6‰ for the subset of RMs between Fe# 0.5 and 1.0.

We have focused here primarily on presenting the first detailed descriptions of $\delta^{18}O$ bias behavior for carbonates of the magnesite-siderite series, and on outlining a functional calibration scheme. The existence at present of two different $\delta^{18}O$ calibration trend types – along with the possibility that more variability in trend shape may be encountered with time – does not limit our ability to make accurate bias corrections (<0.5‰ relative to NIST-19), provided that a sufficient number of reference materials – spanning the range of compositions between magnesite and siderite – are available and utilized each session. Understanding the underlying cause(s) of the complexity we encountered with this solid-solution series, however, requires further study and should perhaps serve as a reminder that calibrating SIMS instruments for analysis of geological materials remains entirely empirical in nature.

The findings of this study stand in contrast to our experience with calibrating the dolomite-ankerite series. The Hill equation introduced previously (Śliwiński et al., 2016a,b) has been applied over a 3-year period using the same curve-shape parameter values to regress calibration data acquired using the same analytical protocols for 3- and 10-µm spot-size $\delta^{18}O$ analysis. Why, then, do these two carbonate solid-solutions behave differently under the same analytical conditions? One possibility is that the $\delta^{18}O$ bias response is insensitive to slight session-specific differences in instrument tuning below some threshold Fe (+Mn?) concentration. Consider the dolomite-ankerite calibration data compared with that of the magnesite-siderite series shown in Fig. 3a (note that composition is expressed here as a molar ratio of Fe+Mn to the sum total of Ca, Mg, Fe and Mn [*i.e.,* $X_{(Fe+Mn)}$] to account for the fact that Ca ideally occupies one-half of all cation sites in the dolomite structure). The Fe-content of our dolomite-ankerite reference materials does not extend into the compositional field where Type-I and -II $\delta^{18}O$ bias trends of the magnesite-siderite series diverge in shape (note that the maximum Fe-content of naturally-occurring ankerites seems to be limited to $X_{(Fe+Mn)} \approx 0.4$; *e.g.,* Change et al., 1996).

Something of potential interest to note here in moving forward is that certain electro-magnetic properties of carbonate minerals vary by several orders of magnitude as a function of Fe+Mn content. One example is electrical resistivity (2×10^{12} *vs.* 70 mΩ for calcite and siderite, respectively; *e.g.,* Telford et al., 1990). Another is magnetic susceptibility (MS), which increases by a factor of 100 between dolomite and ankerite, compared to a factor of 1000 between magnesite and siderite (Fig. 3b; see *e.g.,* Hunt et al., 1995; Rochette, 1988; Schmidt et al., 2006, 2007). We can speculate that properties of this nature make the magnesite-siderite series more sensitive to session-specific differences in tuning of the instrument – which can manifest as differences in pit morphology (Figs. SA 3-6 and 3-7) – by influencing the behavior of the electron cloud which provides charge compensation during sputtering (and its role in promoting the formation of secondary oxygen ions).

A potentially promising direction for future studies is an assessment of how bias trends differ in shape (if at all) when the spot-size is intentionally made smaller or larger by ~25-50% under otherwise routine $\delta^{18}O$ analysis conditions where the target spot-size is 10-µm, for example. Using a primary beam of the same intensity and a fixed analysis time, this would necessarily force a change in the pit depth for a given carbonate composition (to maintain a constant volume of sputtered material). A natural extension of such experiments would be a rigorous assessment of sputtering rates for the different common Ca-Mg-Fe carbonate minerals. In light of analogous studies in silicate systems (*e.g.,* Eiler et al., 1997b, Isa et al., 2017), this could significantly improve our understanding of what drives the first-order differences of ~10-20‰ in bias magnitude between the end-members of the dolomite-ankerite and magnesite-siderite solid-solution series.

We next continue our discussion of $\delta^{18}O$ matrix effects by briefly examining how some of the base signals associated with Type-I and -II calibration trends differ as a function of RM composition. We looked into how Fe# affects $^{16}O^-$ ion yields and the magnitude of drift in the raw isotope ratio over the course of a single spot-analysis. This provides further insight into the circumstances under which inflection points appear in calibration curves, and may be of use in designing further experimental studies seeking to suppress this complexity. No comprehensive model based on first principles exists at present for accurately predicting secondary ion yields from geological materials (and hence the bias imparted to isotope ratios during sputtering). An important component of developing and testing such models, however, is a clear empirical understanding of how base signals vary as a function of composition for solid-solution mineral series under different analytical conditions (consider, for example, the work of Riciputi et al., 1998).

4.3.3.1. Dependence of $^{16}O^-$ ion yield on Fe#

The shape of ion yield *vs.* Fe# trends responds to session-specific differences in tuning. Under both small and large-spot conditions, ion yields were always smallest from magnesite and increased as a function of Fe-content out to Fe# = 0.645; from here, yields either continued increasing out to the siderite end-member (Type-II trends) or began a gradual decline (Type-I trends; 5 to 10% decrease relative to the maximum value at Fe# 0.645 under large- and small-spot conditions, respectively). In more detail:

Under 10-µm spot-size conditions, ion yield trends associated with Type-I and -II $\delta^{18}O$ bias calibrations followed different trajectories (parabolic *vs.* sigmoidal, respectively; see Fig. 4a and additional examples in Fig. SA 3-8). The ion yields of Type-I trends varied by ~1 Gcps/nA between the end-members of the solid-solution, whereas the difference associated with the one example of a Type-II trend observed under these conditions was twice as large. Qualitatively, the rate of change in ion yield was similar for both trend types between Fe# 0.105 and 0.645 but differed considerably near the end-member compositions, where the steeper slopes seen in the Type-II trend resulted in a comparatively higher ion yield from siderite (by ~0.5 Gcps/nA, a ~15% difference) and a lower yield from magnesite (by ~0.3 Gcps/nA, also a ~15% difference).

Under 3-µm spot-size conditions, the ion yield trends associated with both bias calibrations followed parabolic trajectories with maxima at different compositions (at Fe# 0.645 for the Type-I trend and at the siderite-end member for the Type-II trend; Fig. 4b). In both cases count-rates varied by 1.3 Mcps/nA Qualitatively, the rate of change in ion yield was similar between Fe# 0.105 and 0.645; however, a steepening of slope associated with the Type-II trend below Fe# 0.105 (analogous to that observed under large-spot conditions) resulted in a comparatively lower ion yield from magnesite (by ~0.3 Gcps/nA, a change of ~14.5%). Because the two trends crest as different compositions, a count-rate difference of 0.15 Gcps/nA (a ~6% difference) was observed from the siderite end-member.

Note that in the case of Type-II bias calibrations under both small- and large-spot analysis conditions, the ion yield a function of Fe# and Fe# is a function of ion yield (Fig. 4a and b). Thus, hypothetically, the Fe# of a sample material under the beam could be estimated from its ion yield (and this then fed into a Fe# *vs.* bias calibration to determine the appropriate matrix correction factor). Whereas this is not the case for Type-I bias calibrations, the very fact that the shape of ion yield *vs.* Fe# trends responds to session-specific differences in tuning hints at a potential analytical advantage that could be gained through further refinements in technique.

4.3.3.2. Cumulative change in $\delta^{18}O_{raw}$ during sputtering as a function of Fe#

The raw $\delta^{18}O$ value reported for each analysis spot is an average of multiple data collection cycles (20 cycles of 4 seconds each and 25 cycles of 8 seconds under 10- and 3-µm spot-size conditions, respectively). It is thus possible to assess if/how the raw signal changes during sputtering, and if the magnitude of this change is systematically related to composition. Repeat measurements of each RM were therefore summarized on a cycle-by-cycle basis, where all cycle 1 measurements were compiled and averaged, followed by all cycle 2 measurements, etc. Plotting this data shows linear trends towards lower $\delta^{18}O$ values with each passing cycle under both sets of analytical conditions (*i.e.,* fractionation in favor of the lighter isotope increases with time; see cycle-by-cycle plots in Figs. SA 3-9 to 3-12). The cumulative change in $\delta^{18}O_{raw}$ between the first and last cycle of analysis ("$\Delta^{18}O(c_f - c_i)$") shows a dependence on composition (the terms *"c_i"* and *"c_f"* respectively refer to the initial and final cycles). In a qualitative sense, the dependence of $\Delta^{18}O(c_f - c_i)$ on Fe# follows well- to moderately-well defined parabolic trajectories under both large- and small-spot conditions, respectively (Fig. 4c-d). Values of $\Delta^{18}O(c_f - c_i)$ tend to be smallest near the mid-point of the solid-solution (*i.e.,* consider the least negative values in Fig. 4c-d, which represent the least amount of down-pit discrimination against $^{18}O^-$). Values of $\Delta^{18}O(c_f - c_i)$ are largest (*i.e.,* most negative) at the compositional end-members and are of equal- to sub-equal magnitude. If we regard the average $\Delta^{18}O(c_f - c_i)$ value of the magnesite and siderite end-members as a baseline (as frame of reference), then we note the following: 1) the baseline is lower in the case of Type-I (approximately -3.5‰) *vs.* Type-II (approximately -1.5‰) $\delta^{18}O$ bias calibrations under both large- and small-spot conditions (there is necessarily more scatter in the small-spot data due to

comparatively poorer counting statistics); 2) the range of $\Delta^{18}O(c_f - c_i)$ values is somewhat larger in the case of Type-I (approximately 2‰) *vs.* Type-II (approximately 1.5‰) $\delta^{18}O$ bias calibrations under both large- and small-spot conditions (Fig. 4c-d).

In comparing the base signals of Type-I and -II calibration trends and in reflecting on how they affect measured bias values, we observe that the lower ion yields associated with the Type-II trend near the magnesite end-member (Fe# < 0.2) correspond to larger bias values (by up to 6‰; see Fig. 2a). This follows general expectations. Surprisingly, however, larger bias values were also observed near the siderite end-member (Fe# > 0.8; by up to 4‰; Fig. 2a) despite ion yields being higher (compared to the Type-I trend). At the same time, the $\Delta^{18}O(c_f - c_i)$ *vs.* Fe# trends of both $\delta^{18}O$ calibration types are generally comparable beyond a baseline shift (for each trend, note the similar magnitude of $\Delta^{18}O(c_f - c_i)$ for the end-members and the general symmetry of the data distributions in Fig. 4c). Differences in the topology of Type-I *vs.* Type-II bias calibrations do not seem to be readily explainable by considering only a simple interplay between these two base variables (*i.e.,* trends in ion yield and $\Delta^{18}O(c_f - c_i)$ as a function of Fe#). We suspect that differences in sputtering rate contribute here as well, as a visual comparison of pit images (Figs. SA 3-6 and 3-7) suggests that pit depth (and hence sputtering rate) increases with increasing Fe-content. Given what is known from silicate and carbonate systems, bias and sputtering rate can correlate strongly and non-linearly (*e.g.,* Eiler et al., 1997b, Isa et al., 2017). Nonetheless, what is apparent from the data at hand is that above a certain threshold Fe-concentration, carbonate $\delta^{18}O$ bias calibration curve shapes are strongly influenced by session-specific differences in instrument tuning (reflected by the resulting pit morphologies/geometries). Where tuning conditions accentuate differences in base parameters such as ion yield and the observed down-hole drift of the raw isotope ratio during sputtering, the end result is a more complex calibration curve (compare base signals and corresponding bias curves of Type-I and -II trend in Figs. 2 and 4).

4.3.4. The behavior of SIMS $\delta^{13}C$ bias along the magnesite-siderite binary

In all instances (Type-I and II trends), the change in the magnitude of $\delta^{13}C$ bias (un-normalized) between the end-members of the magnesite-siderite solid-solution series is consistently unidirectional (albeit non-linear). Relative to the magnesite end-member, the bias *increases* by ~10‰ as a function of increasing Fe-content (Fig. 5a). In other words, the per mil difference between $\delta^{13}C_{raw}$ as measured by SIMS and the 'accepted' $\delta^{13}C_{VPDB}$ values becomes *larger* (as values became more negative, the bias is said to *increase*). The bias is always *smallest* for end-member magnesite (-51.5 ‰) and different by 10‰ in relation to end-member siderite (approximately -61.5‰) (session S23 data, see also Table 4 and calibrations from other sessions in Fig. SA 3-15). From here on the discussion will focus on *working calibration curves* (Fig. 5b), for which $\delta^{13}C$ bias values have been normalized to that of the magnesite end-member anchor (*i.e.,* values expressed as $\delta^{13}C$ bias*(RM-UWMgs1)).

4.3.4.1. TYPE-I AND II $\delta^{13}C$ TRENDS

The shape of Type-I $\delta^{13}C$ calibrations resembles a gently-flexing 3rd–order polynomial (Fig. 5b; session S23 data). The bias response was most sensitive to changes in cation chemistry in the Fe# range between 0 and 0.3 (change of ~5.5‰ relative to end-member magnesite). Between Fe# 0.3 and 1.0, the change was more gradual (approximately linear), with $\delta^{13}C$ bias*(RM-UWMgs1) values changing by an additional ~5.5‰ over this much broader range of compositions. The data were regressed using equation (6), yielding the following parameter values: n = 1.7 (± 0.1, 2*se*) k = 0.73 (± 0.1, 2*se*), d = 2.4 (± 0.8, 2*se*), $C_1 = C_2$ = -5.1 (± 0.4, 2*se*) and C_3 = 0. This same set of curve shape parameter values was successfully applied in regressing calibration data from one other session that yielded a Type-I trend (Fig. SA 3-15). In both instances, the measured average value of $\delta^{13}C$ bias*(RM-UWMgs1) for all RMs differs by less than 0.5‰ from the output of the calibration model (see residual plots in Figs. 5b and SA 3-15). This can be considered a measure of trueness in relation to CRM NIST-19 (Verkouteren and Klinedinst, 2004). As with $\delta^{18}O$, the calibration residuals show no correlation to calcium (r = 0.03) or manganese (r = 0.15) content, and the calibration remains unchanged with the inclusion of Mn in the Fe# (Fig. SA 3-3). No secondary matrix corrections are thus required for this particular suite of RMs.

In contrast, the shape of Type-II $\delta^{13}C$ calibrations can be adequately described by gently-flexing 2nd-order polynomials, yielding residuals < 0.5‰ (Fig. 5b; session S18 data). The change in bias is thus more gradual when compared to Type-I trends, but is of the same general magnitude (~10‰) across the entire solid-solution series (one additional example is shown in Figure SA 3-15; please note that both examples of Type-I trends represent sessions from earlier stages research when far fewer RMs were available). The shape of both trend types differed most in the compositional space between Fe# = 0 and 0.5, where RM bias values changed on a session-by-session basis by up 1-2‰.

We continue our discussion of $\delta^{13}C$ matrix effects by briefly examining how base signals varied with RM composition. The $^{12}C^-$ ion yields associated with the two different $\delta^{13}C$ bias calibration trend types shown in Figure 5 are plotted as a function of composition in Figure 6a (see also Fig. SA 3-16). The ion yield of the Type-I trend can be described as a parabolic function of Fe# that is symmetric around the midpoint composition of the solid-solution, where it achieves a maximum value of ~12.5 Mcps/nA. Count rates were lowest and of the same general magnitude from the compositional end-members (~8 Mcps/nA). The ion yield of the Type-II trend also followed a parabolic trajectory with a maximum near the compositional midpoint (~13 Mcps/nA), although the count-rates measured from the end-members were dissimilar (~9 and 8 Mcps/nA for magnesite and siderite, respectively).

In evaluating the change in $\delta^{13}C_{raw}$ across the 20 data acquisition cycles associated with each individual spot analysis, we noted moderately-well defined linear trends toward lower values in both Type-I and -II bias calibration datasets (*i.e.,* fractionation in favor of the lighter isotope increased with time; see cycle-by-cycle plots in Figs. SA 3-17 and 3-20). Considering that the spot-to-spot repeatability of a $\delta^{13}C$ analysis is on the order of 0.6-1.2‰ (2*s*), the

cumulative change in $\delta^{13}C_{raw}$ between the first and last cycle of analysis ("$\Delta^{13}C(c_f - c_i)$") shows no resolvable dependence on Fe# in the case of the Type-II bias trend (average change of -4‰). In contrast, a weak parabolic dependence was noted in association with the Type-I trend, where the cumulative change in $\Delta^{13}C(c_f - c_i)$ is smallest near the compositional midpoint of the solid-solution (approximately -2‰) and largest near the end-members (approximately -4‰; see Fig. 6b and additional examples from other sessions in Fig. SA 3-16b).

5. Conclusions and recommendations

Recent advances in SIMS instrument design and refinements of analytical techniques have brought about the technical capability of performing highly precise, micrometer-scale in-situ measurements of carbonate $\delta^{18}O$ and $\delta^{13}C$ values. The common spot-sizes employed for $\delta^{18}O$ analyses at WiscSIMS are either of a 3 or 10-µm diameter, affording repeatability at the following levels: ±0.3‰ (2*s*; 10-µm spots) and ±0.7‰ (2*s*; 3-µm spots). A 6-µm spot is used for $\delta^{13}C$ analyses, with repeatability between 0.6 and 1.2‰ (2*s*).

The accuracy of such measurements in relation to certified reference materials, however, depends in large-part on the availability of comprehensive suites of matrix-matched reference materials that allow for characterizing and calibrating sample matrix effects. This is entirely an empirical undertaking. With regards to Ca-Mg-Fe carbonates, this has been an under-researched topic since the first pioneering studies in the late 1990's (*e.g.,* Eiler et al., 1997a; Valley et al., 1997; Riciputi et al., 1998). With this 3rd installment of our on-going study of these effects, most of the common inorganic Ca-Mg-Fe carbonate compositions can now be accurately analyzed. This includes calcite (Kozdon et al., 2009) and both the dolomite-ankerite (Parts I and II; Śliwiński et al., 2016a, 2016b) and magnesite-siderite solid-solution series (Part III, this article). Biogenic carbonates may present additional complexity if organic matter, water or fine-grained textures are present (Orland et al. 2015).

Following two years of RM development and of acquiring calibration datasets, we can at present offer the following observations, conclusions or recommendations regarding SIMS analysis of carbonates of the magnesite-siderite series:

1. As with the dolomite-ankerite series, mass bias was consistently most sensitive to changes in composition near the iron-free end-member of the solid-solution. With increasing Fe-content up to ~20 mol% $FeCO_3$ end-member (Fe# 0-0.2, where Fe# = Fe/(Mg+Fe), expressed on a molar basis), $\delta^{13}C$ bias *increased* by up to 3-4.5‰, whereas $\delta^{18}O$ bias *decreased* by 13-15‰ (session-specific differences).
2. Between the end-members of the series, $\delta^{13}C$ bias increased by a total of 10-11‰ (magnesite→siderite), whereas $\delta^{18}O$ bias decreased by 13-16‰ (session-specific differences).
3. As an example, if uncorrected, the presence of 1-2 mol% $FeCO_3$ in a sample material of unknown isotopic composition would produce a measurement error (in relation to CRM NIST-19) of ~1‰ for $\delta^{13}C$ and ~2-3‰ for $\delta^{18}O$ measurements.

4. Despite adherence to well-established analytical protocols for carbonate $\delta^{13}C$ and $\delta^{18}O$ analyses at WiscSIMS (CAMECA IMS 1280), the magnesite-siderite calibration curves of both isotope systems did not maintain a constant shape from session-to-session over a 2-year period, but rather fell into one of two distinct and largely self-consistent shape-categories ('Type-I' and 'Type-II').
5. The shape of Type-I and II $\delta^{18}O$ bias trends differs most in the compositional space between Fe# = 0.3 and 0.9, where RM bias values changed on a session-by-session basis by: 1) up to 6‰ when using conditions for 10-µm diameter spot-size measurements; and 2) up to 4‰ when using 3-µm conditions
6. The shape of Type-I and II $\delta^{13}C$ bias trends differ most in the compositional space between Fe# = 0 and 0.5, where RM bias values change on a session-by-session basis by up 1-2‰.
7. The cause of variability in calibration curve shapes is not well understood at present, and stresses the importance of having available a sufficient number of well-characterized RMs so that potential complexities of curvature can be adequately delineated and accounted for on a session-by-session basis. Doing so allows for calibration residuals (a measure of accuracy in relation to CRM NIST-19) smaller than 0.5‰ for both isotope systems.

Acknowledgments

This material is based primarily upon work supported by the US Department of Energy Office of Science, Office of Basic Energy Sciences, Chemical Sciences, Geosciences, and Biosciences Division under award number DE-FG02-93ER14389. The WiscSIMS Laboratory is partly funded by the US National Science Foundation (EAR-1355590) and the University of Wisconsin- Madison. We express our gratitude to University of Wisconsin-Madison colleagues: N. Kita for providing guidance on SIMS analysis, J. Kern for instrumentation support, P. Sobol for constructive discussions and W. Schneider for assistance with SEM imaging. We warmly thank the following individuals and institutions for facilitating this research by supplying many of the mineral specimens that were assessed during the first three parts of this study, some of which were successfully developed into reference materials: P.W. Pohwat and the Smithsonian Institution (source of UWMgs6 [NMNH 96962] and UWAnk4 [NMNH 93418-08]), R.S. Bottrill and Mineral Resources Tasmania (source of UWMgs7), J.M. Eiler (material for UWSd5/JE-Mg-Sid and UWAnk7), J. Craven (material for UWSd1 / Ivig. Sid) and Josef Huber (http://www.hubermineralien.jimdo.com), who located and supplied the source materials for the RMs UWAnk5cl, -5opq, -6a, and UWMgs2 and -3. We thank two anonymous reviewers for a constructive review of this work.

REFERENCES

Allison C. E., Francey R. J. and Meijer H. A. J. (1995)
Reference and intercomparison materials for stable isotopes of light elements
IAEA-TECDOC, 825, 155-162.

Baertschi P. (1976)
Absolute ^{18}O content of standard mean ocean water.
Earth and Planetary Science Letters, 31, 341–344.

Beukes N.J. and Klein C. (1990)
Geochemistry and sedimentology of a facies transition — from microbanded to granular iron-formation — in the early Proterozoic Transvaal Supergroup, South Africa. Precambrian Research 47, 99–139.

Beukes N.J., Klein C., Kaufman A.J. and Hayes J.M. (1989)
Carbonate petrography, kerogen distribution, and carbon and oxygen isotope variations in an early Proterozoic transition from limestone to iron-formation deposition, Transvaal Supergroup, South Africa. Economic geology and the bulletin of the Society of Economic Geologists 85, 663–690.

Blake D.F., Amundsen H.E.F., Benning L., Bish D., Conrad P., Fogel M., Midtkandal I., Ming D., Steele A., Treiman A.H. and AMASE team (2010)
Carbonate Cements from the Sverrefjell and Sigurdfjell Volcanoes, Svalbard Norway; Terrestrial Analogs for Martian Carbonates? LPI Contributions 1538, 5119.

Botz R.W. and von der Borch C.C. (1984)
Stable isotope study of carbonate sediments from the Coorong Area, South Australia. Sedimentology 31, 837–849.

Brodie M.W. (2016)
Diagenesis & Reservoir Quality of the Middle Bakken Formation. Doctoral thesis, Durham University

Buckley H.A. and Woolley, A.R. (1990)
Carbonates of the magnesite–siderite series from four carbonatite complexes. Mineralogical Magazine 54, 413–418.
Burley, S.D., Worden, R.H., 2003. Sandstone diagenesis: recent and ancient. Blackwell Pub., Malden, MA.

Chai L. and Navrotsky A. (1996)
Synthesis, characterization, and enthalpy of mixing of the $(Fe,Mg)CO_3$ solid solution. Geochimica et Cosmochimica Acta 60, 4377–4383.

Chang L.L., Howie R.A. and Zussman J. (1996)
Rock forming minerals, Volume 5B: Non-Silicates: Sulphates, carbonates, phosphates, halides. Longman (Harlow, Essen), 383pp.

Coplen, T.B., Kendall C. and Hopple J. (1983)
Comparison of stable isotope reference samples. Nature 302, 236-238

Craig H. (1957)
Isotopic standards for carbon and oxygen and correction factors for mass-spectrometric analysis of carbon dioxide. Geochimica et Cosmochimica Acta 12, 133–149.

Curtis C., Petrowski C. and Oertel G. (1972)
Stable carbon isotope ratios within carbonate concretions - clue to place and time of formation. Nature 235, 98-100.

Curtis C.D. (1995)
Post-depositional evolution of mudstones l: early days and parental influences. Journal of the Geological Society 152, 577–586.

Curtis C.D., Coleman M.L. and Love L.G., (1986)
Pore water evolution during sediment burial from isotopic and mineral chemistry of calcite, dolomite and siderite concretions. Geochimica et Cosmochimica Acta 50, 2321–2334.

Dobrzhinetskaya L.F., Green H.W., Mitchell T.E. and Dickerson R.M. (2001)
Metamorphic diamonds: mechanism of growth and inclusion of oxides. Geology 29, 263–266.

Donovan J. J., Kremser D. and Fournelle J. H. (2007)
ProbeForWindows User's Guide and Reference, Enterprise Edition. Probe Software, Inc, Eugene, OR 355 p.

Donovan J.J. and Tingle T.N. (1996)
An improved mean atomic number background correction for quantitative microanalysis. Microscopy and Microanalysis 2(1), 1-7

Dworkin S.I., Nordt L. and Atchley S. (2005)
Determining terrestrial paleotemperatures using the oxygen isotopic composition of pedogenic carbonate. Earth and Planetary Science Letters 237, 56–68.

Eiler J.M., Valley J.W. and Graham C.M. (1997a)
Standardization of SIMS analysis of O and C isotope ratios in carbonates from ALH84001. 28th Annual Lunar and Planetary Science Conference, 327p.

Eiler J.M., Graham C. and Valley J.W. (1997b)
SIMS analysis of oxygen isotopes: matrix effects in complex minerals and glasses. Chemical Geology 138, 221–244.

Eiler J.M., Valley J.W., Graham C.M. and Fournelle J. (2002)
Two populations of carbonate in ALH84001: Geochemical evidence for discrimination and genesis. Geochimica et Cosmochimica Acta 66, 1285–1303.

Fàbrega C., Parcerisa D., Rossell J.M., Gurenko A. and Franke C. (2017)
Predicting instrumental mass fractionation (IMF) of stable isotope SIMS analyses by response surface methodology (RSM). Journal of Analytical Atomic Spectrometry, 32, 731-748.

Fayek M., Harrison T.M., Grove M., McKeegan K.D., Coath C.D. and Boles J.R. (2001)
In situ stable isotopic evidence for protracted and complex carbonate cementation in a petroleum reservoir, North Coles Levee, San Joaquin Basin, California, USA. Journal of Sedimentary Research 71, 444–458.

Fernández-Nieto C., Torres-Ruiz J., Pérez I.S., González I.F. and López J.G. (2003)
Genesis of Mg-Fe carbonates from the Sierra Menera magnesite-siderite deposits, Northeast Spain: Evidence from Fluid inclusions, Trace elements, rare earth elements, and stable isotope data. Economic Geology 98, 1413–1426.

Fitzsimons I.C.W., Harte B. and Clark R.M. (2000)
SIMS stable isotope measurement: counting statistics and analytical precision. Mineralogical Magazine 64, 59–83.
Frost M.T. (1982)
The magnesite deposit at Main Creek, Savage River, Tasmania. Economic Geology 77, 1901–1911.

Gautier D.L. (1982)
Siderite concretions: indicators of early diagenesis in the Gammon Shale (Cretaceous). Journal of Sedimentary Research 52(3), 0859-0871.

Goutelle S., Maurin M., Rougier F., Barbaut X., Bourguignon L., Ducher M. and Maire P., (2008)
The Hill equation: a review of its capabilities in pharmacological modelling. Fundamental & Clinical Pharmacology 22, 633–648.

Haroldson E.L. (2017)
Fluid inclusion and stable isotope study of Magino: a magmatic related Archean gold deposit. Doctoral thesis, University of Wisconsin-Madison

Heimann A., Johnson C.M., Beard B.L., Valley J.W., Roden E.E., Spicuzza M.J. and Beukes N.J., (2010)
Fe, C, and O isotope compositions of banded iron formation carbonates demonstrate a major role for dissimilatory iron reduction in ~2.5 Ga marine environments. Earth and Planetary Science Letters 294, 8–18.

Hervig R.L., Williams P., Thomas R.M., Schauer S.N. and Steele I.M. (1992)
Microanalysis of oxygen isotopes in insulators by secondary ion mass spectrometry. International Journal of Mass Spectrometry and Ion Processes 120, 45–63.

Hill A.V. (1910)
The Possible Effects of The Aggregation of The Molecules of Haemoglobin on its Dissociation Curves. The Journal of Physiology 40, iv–vii.

Huberty J.M., Kita N.T., Kozdon R., Heck P.R., Fournelle J.H., Spicuzza M.J., Xu H. and Valley J.W. (2010)
Crystal orientation effects in $\delta^{18}O$ for magnetite and hematite by SIMS. Chemical Geology 276, 269–283.

Hunt C.P., Moskowitz B.M. and Banerjee S.K. (1995)
Magnetic properties of rocks and minerals. *In* Rock Physics and Phase Relations. A Handbook of Physical Constants. AGU Reference Shelf
Ickert R.B. and Stern R.A. (2013)
Matrix Corrections and Error Analysis in High-Precision SIMS $^{18}O/^{16}O$ Measurements of Ca-Mg-Fe Garnet. Geostandards and Geoanalytical Research 37, 429–448.

Isa J., Kohl I.E., Liu M.-C., Wasson J.T., Young E.D. and McKeegan K.D. (2017)
Quantification of oxygen isotope SIMS matrix effects in olivine samples: Correlation with sputter rate. Chemical Geology 458, 14-21

James H.L. (1954)
Sedimentary facies of iron-formation. Economic Geology 49, 235–293.

Johnson C.M., Ludois J.M., Beard B.L., Beukes N.J. and Heimann A. (2013)
Iron formation carbonates: Paleoceanographic proxy or recorder of microbial diagenesis? Geology 41, 1147–1150.

Kaminsky F.V., Wirth R. and Schreiber A. (2013a)
Carbonatitic inclusions in deep mantle diamond from Juina, Brazil: New minerals in the carbonate-halide association. The Canadian Mineralogist 51, 669–688.

Kaufman A., Hayes J. and Klein, C. (1990)
Primary and Diagenetic Controls of Isotopic Compositions of Iron-Formation Carbonates. Geochimica Et Cosmochimica Acta 54, 3461–3473.

Kim S., Mucci A. and Taylor B.E. (2007)
Phosphoric acid fractionation factors for calcite and aragonite between 25 and 75 °C: Revisited. Chemical Geology 246, 135-146

Kita N.T., Huberty J.M., Kozdon R., Beard B.L. and Valley J.W. (2011)
High-precision SIMS oxygen, sulfur and iron stable isotope analyses of geological materials: accuracy, surface topography and crystal orientation. Surface and Interface Analysis 43, 427–431.

Kita N.T., Ushikubo T., Fu B. and Valley J.W. (2009)
High precision SIMS oxygen isotope analysis and the effect of sample topography. Chemical Geology 264, 43–57.

Kitajima K., Strickland A., Spicuzza M.J. and Valley J.W. (2015)
Improvement in matrix correction of $\delta^{18}O$ analysis by SIMS for pyralspite and Cr-pyrope garnet. Presented at the High Resolution Proxies of Paleoclimate (HiRes2015), WiscSIMS Laboratory, University of Wisconsin-Madison.

Klein C. (2005)
Some Precambrian banded iron-formations (BIFs) from around the world: Their age, geologic setting, mineralogy, metamorphism, geochemistry, and origins. American Mineralogist 90, 1473–1499.

Kozdon R., Ushikubo T., Kita N.T., Spicuzza M. and Valley J.W. (2009)
Intratest oxygen isotope variability in the planktonic foraminifer N. pachyderma: Real vs. apparent vital effects by ion microprobe. Chemical Geology 258, 327–337.

Ludvigson G.A., Gonzalez L.A., Fowle D.A., Roberts J.A., Driese S.G., Villarreal M.A., Smith J.J. and Suarez M.B. (2013)
Paleoclimatic applications and modern process studies of pedogenic siderite, *In*: Driese, S.G., Nordt, L.C. (Eds.), New Frontiers in Paleopedology and Terrestrial Paleoclimatology: Paleosols and Soil Surface Analog Systems. SEPM, Tulsa, 79–87pp.

Ludvigson G.A., González L.A., Metzger R.A., Witzke B.J., Brenner R.L., Murillo A.P. and White T.S. (1998)
Meteoric sphaerosiderite lines and their use for paleohydrology and paleoclimatology. Geology 26, 1039–1042.

Lugli S., Morteani G. and Blamart D. (2002)
Petrographic, REE, fluid inclusion and stable isotope study of magnesite from the Upper Triassic Burano Evaporites (Secchia Valley, northern Apennines): contributions from sedimentary, hydrothermal and metasomatic sources. Mineralium Deposita 37, 480–494.

Luzón A., Mayayo M.J. and Pérez A. (2009)
Stable isotope characterisation of co-existing carbonates from the Holocene Gallocanta lake (NE Spain): palaeolimnological implications. International Journal of Earth Sciences 98, 1129–1150.

Macquaker J.H.S., Curtis C.D. and Coleman M.L. (1997)
The role of iron in mudstone diagenesis; comparison of Kimmeridge Clay Formation mudstones from onshore and offshore (UKCS) localities. Journal of Sedimentary Research 67, 871–878.

Mayayo M.J., Bauluz B., López-Galindo A. and González-López J.M. (1996)
Mineralogy and geochemistry of the carbonates in the Calatayud Basin (Zaragoza, Spain). Chemical Geology 130, 123–136.

Mees F. and Keppens E. (2013)
Stable isotope geochemistry of magnesite from Holocene salt lake deposits, Taoudenni, Mali. Geol. J. 48, 620–627.

McCrea J.M. (1950)
On the Isotopic Chemistry of Carbonates and a Paleotemperature Scale. The Journal of Chemical Physics 18, 849.

McGrail B.P., Schaef H.T., Spane F.A., Cliff J.B., Qafoku O., Horner J.A., Thompson C.J., Owen A.T. and Sullivan C.E. (2016)
Field Validation of Supercritical CO_2 Reactivity with Basalts. Environmental Science & Technology Letters, 4(1), 6-10.

Morad S. (1998)
Carbonate Cementation in Sandstones: Distribution Patterns and Geochemical Evolution, *In*: Morad, S. (Ed.), Carbonate Cementation in Sandstones. Blackwell Publishing Ltd., 1–26.

Morris R.V., Blake D.F., Bish D., Ming D.W., Agresti D.G., Treiman A.H., Steele A. and Amundsen H.E.F. (2011)
A Terrestrial Analogue from Spitsbergen (Svalbard, Norway) for the Comanche Carbonate at Gusev Crater, Mars. LPI Contribution No. 1608, 1699p.

Mozley P.S. (1989a)
Complex compositional zonation in concretionary siderite; implications for geochemical studies. Journal of Sedimentary Research 59, 815–818.

Mozley P.S. (1989b)
Relation between depositional environment and the elemental composition of early diagenetic siderite. Geology 17, 704–706.

Niles P.B., Catling D.C., Berger G., Chassefière E., Ehlmann B.L., Michalski J.R., Morris R., Ruff S.W. and Sutter B. (2013)
Geochemistry of Carbonates on Mars: Implications for Climate History and Nature of Aqueous Environments. Space Science Reviews 174, 301–328.

Orland I. J., Kozdon R., Linzmeier B., Wycech J., Śliwiński M., Kitajima K., Kita N. T. and Valley J.W. (2015)
Enhancing the accuracy of carbonate $\delta^{18}O$ and $\delta^{13}C$ measurements by SIMS, Paper Number: PP52B-03, AGU Fall 2015 Meeting, Dec. 18 2015, San Francisco CA.

Page F.Z., Kita N.T. and Valley J.W. (2010)
Ion microprobe analysis of oxygen isotopes in garnets of complex chemistry. Chemical Geology 270, 9-19.

Perry E.C., Tan F.C. and Morey G.B. (1973)
Geology and stable isotope geochemistry of the Biwabik Iron Formation, northern Minnesota. Economic Geology 68, 1110–1125.

Postma D. (1982)
Pyrite and siderite formation in brackish and freshwater swamp sediments. Am J Sci 282, 1151–1183.

Power I. and Southam G. (2005)
Carbon dioxide sequestration through enhanced weathering of chrysotile mine tailings and subsequent microbial precipitation of magnesium carbonates. Geochimica et Cosmochimica Acta Supplement 69, 834.

Power I.M., Harrison A.L., Dipple G.M., Wilson S.A., Kelemen P.B., Hitch M. and Southam, G. (2013)
Carbon Mineralization: From Natural Analogues to Engineered Systems. Reviews in Mineralogy and Geochemistry 77, 305–360.

Rochette P. (1988)
Inverse magnetic fabric in carbonate-bearing rocks. Earth and Planetary Science Letters 90, 229-237

Riciputi L.R., Paterson B.A. and Ripperdan R.L. (1998)
Measurement of light stable isotope ratios by SIMS: Matrix effects for oxygen, carbon, and sulfur isotopes in minerals. International Journal of Mass Spectrometry 178, 81–112.

Rollion-Bard C. and Marin-Carbonne, J. (2011)
Determination of SIMS matrix effects on oxygen isotopic compositions in carbonates. Journal of Analytical Atomic Spectrometry 26, 1285.

Rosenbaum J. and Sheppard S.M.F. (1986)
An isotopic study of siderites, dolomites and ankerites at high temperatures. Geochimica et Cosmochimica Acta 50, 1147–1150.

Sanz-Montero M.E. and Rodríguez-Aranda J.P. (2012)
Magnesite formation by microbial activity: Evidence from a Miocene hypersaline lake. Sedimentary Geology, Signatures of Microbes and Microbial Mats and the Sedimentary Record 263–264, 6–15.

Schmidt V., Günther D. and Hirt A.M. (2006)
Magnetic anisotropy of calcite at room-temperature. Tectonophysics 418, 63-73

Schmidt V., Hirt A.M., Hametner K. and Günther (2007) Magnetic anisotropy of carbonate minerals at room temperature and 77K. American Mineralogist 92, 1673-1684

Sheldon N.D. and Tabor N.J. (2009)
Quantitative paleoenvironmental and paleoclimatic reconstruction using paleosols. Earth-Science Reviews 95, 1–52.

Śliwiński M.G., Kitajima K., Kozdon R., Spicuzza M.J., Denny A. and Valley J.W. (2017)
In situ $\delta^{13}C$ and $\delta^{18}O$ microanalysis by SIMS: A method for characterizing the carbonate components of natural and engineered CO_2-reservoirs. International Journal of Greenhouse Gas Control, 57, 116–133.

Śliwiński M.G., Kitajima K., Kozdon R., Spicuzza M.J., Fournelle J.H., Denny A. and Valley J.W. (2016a)
Secondary Ion Mass Spectrometry Bias on Isotope Ratios in Dolomite–Ankerite, Part I: $\delta^{18}O$ Matrix Effects. Geostandards and Geoanalytical Research, 40, 157–172.

Śliwiński M.G., Kitajima K., Kozdon R., Spicuzza M.J., Fournelle J.H., Denny A. and Valley J.W. (2016b)
Secondary Ion Mass Spectrometry Bias on Isotope Ratios in Dolomite–Ankerite, Part II: $\delta^{13}C$ Matrix Effects. Geostandards and Geoanalytical Research, 40, 173–184.

Sobolev N.V., Kaminsky F.V., Griffin W.L., Yefimova E.S., Win T.T., Ryan C.G. and Botkunov, A.I. (1997)
Mineral inclusions in diamonds from the Sputnik kimberlite pipe, Yakutia. Lithos 39, 135–157.

Stern J.C., McAdam A.C., Ten Kate I.L., Bish D.L., Blake D.F., Morris R.V., Bowden R., Fogel M.L., Glamoclija M., Mahaffy P.R., Steele A. and Amundsen H.E.F. (2013)
Isotopic and geochemical investigation of two distinct Mars analog environments using evolved gas techniques in Svalbard, Norway. Icarus 224, 297–308.

Suarez, M.B., González, L.A., Ludvigson, G.A. (2010)
Estimating the oxygen isotopic composition of equatorial precipitation during the mid-Cretaceous. Journal of Sedimentary Research 80, 480–491.

Telford W., Geldart L. and Sheriff R. (1990)
Electrical Properties of Rocks and Minerals. *In* Applied Geophysics. Cambridge: Cambridge University Press., pp. 283-292
doi:10.1017/CBO9781139167932.009

Tabor N.J. and Myers T.S. (2015)
Paleosols as indicators of paleoenvironment and paleoclimate. Annual Review of Earth and Planetary Sciences 43, 333–361.

Treiman A.H., Amundsen H.E., Blake D.F. and Bunch T. (2002)
Hydrothermal origin for carbonate globules in Martian meteorite ALH84001: a terrestrial analogue from Spitsbergen (Norway). Earth and Planetary Science Letters 204, 323–332.

Ufnar D.F., González L.A., Ludvigson G.A., Brenner R.L. and Witzke B.J. (2004)
Diagenetic overprinting of the sphaerosiderite palaeoclimate proxy: are records of pedogenic groundwater $\delta^{18}O$ values preserved? Sedimentology 51, 127–144.

Valley J.W., Eiler J.M., Graham C.M., Gibson E.K., Romanek C.S. and Stolper E.M. (1997)
Low-temperature carbonate concretions in the Martian meteorite ALH84001: Evidence from stable isotopes and mineralogy. Science, 275, 1633-1638

Valley J.W. and Kita N.T. (2009)
In situ oxygen isotope geochemistry by ion microprobe, *In*: Fayek, M. (Ed.), Secondary Ion Mass Spectrometry in the Earth Sciences: Gleaning the Big Picture from a Small Spot. Mineralogical Association of Canada (MAC), pp. 19–63.

VIM (2008)
International vocabulary of metrology – Basin and general concepts and associated terms (VIM).

Joint Committee for Guides in Metrology, Bureau International des Poids et Mesures (Sévres, France), 200:2008, 90pp.

Verkouteren R.M. and Klinedinst D.B. (2004)
Value assignment and uncertainty estimation of selected light stable isotope reference materials. NIST SPECIAL PUBLICATION 260, 149.

Wang A., Pasteris J.D., Meyer H.O.A. and Dele-Duboi M.L. (1996)
Magnesite-bearing inclusion assemblage in natural diamond. Earth and Planetary Science Letters 141, 293–306.

Wilson S.A., Dipple G.M., Power I.M., Thom J.M., Anderson R.G., Raudsepp M., Gabites J.E. and Southam G. (2009)
Carbon dioxide fixation within mine wastes of ultramafic-hosted ore deposits: Examples from the Clinton Creek and Cassiar chrysotile deposits, Canada. Economic Geology 104, 95–112.

FIGURE AND TABLE CAPTIONS

Figure 1. Ternary diagram showing the range of Ca-Mg-Fe carbonate compositions represented by the microanalytical reference materials developed at WiscSIMS for calibrating SIMS $\delta^{18}O$ and $\delta^{13}C$ analyses (Table 1): magnesite-siderite series (this study); dolomite-ankerite series (reported in Śliwiński et al., 2016a, 2016b), and calcite UWC-3 (Kozdon et al., 2009). Symbols represent average values (associated *2se* values smaller than symbols).

Fig. 2. (a-b) Plot relating SIMS $\delta^{18}O$ bias (‰) to the cation composition of carbonates belonging to the siderite-magnesite solid solution series [Fe# = Fe/(Mg+Fe), molar]. Shown are representative examples of two types of bias behavior observed using consistent analytical protocols for: **(a)** 10-µm diameter spot-size measurements and **(b)** 3-µm measurements. **(c-d)** Working calibration curves based on the data plotted in **(a-b)**, where bias values are normalized to end-member magnesite (expressed as $\delta^{18}O$ bias*(RM-UWMgs1)), which serves as the calibration anchor. Immediately below are the calibration residuals, which can be considered a measure of accuracy relative to the CRM NIST-19. (Refer to Supplementary Appendix 3 for additional calibration examples).

Fig. 3. (a) A comparison of SIMS $\delta^{18}O$ bias measured from carbonates of the dolomite-ankerite and magnesite-siderite solid-solution series using the same conditions during a single analytical session (asterisks indicates a modeled bias value; refer to Fig. SA 3-2b). Composition is plotted here as a molar ratio of Fe+Mn to the sum of all cations (*i.e.,* $X_{(Fe+Mn)}$) to facilitate comparison with data in **(b),** which shows systematic changes in the magnetic susceptibility (MS) of carbonates as a function of Fe+Mn concentration (data from: [1,2] Schmidt et al., 2007; [3] Schmidt et al., 2006; [4] Rochette 1988). Note that the Fe+Mn content of the dolomite-ankerite RM suite (Śliwiński et al., 2016a) does not extend far into the compositional field where Type-I and -II bias trends of the magnesite-siderite series begin to diverge in shape ($X_{(Fe+Mn)} > \sim 0.3$; see Fig. SA 3-5), suggesting that the $\delta^{18}O$ bias response is insensitive to slight session-specific differences in instrument tuning below this threshold (*i.e.,* differences in trend shape are not expected for the dolomite-ankerite series and indeed have not been observed over the last 3-year period).

Fig. 4. The compositional dependence of certain base signals associated with SIMS $\delta^{18}O$ bias measurements from the magnesite-siderite series. **(a-b)** Secondary $^{16}O^-$ ion yields *vs.* Fe# and **(c-d)** the cumulative change in $\delta^{18}O_{raw}$ between the initial (*i*) and final (*f*) cycles of analysis ("$\Delta^{18}O(c_f - c_i)$") *vs.* Fe# for both 10- and 3-µm spot-size analysis conditions. Yield = count rate (as giga-counts per second) / primary Cs^+ ion beam intensity (nA). Each point is an average of at least 4 measurements from 4 separate grains (1 analysis/grain). (See text for description of 'Type-I' *vs.* 'Type-II' bias trends).

Fig. 5. (a) Plot relating SIMS $\delta^{13}C$ bias (‰) to the cation composition of carbonates belonging to the siderite-magnesite solid solution series [Fe# = Fe/(Mg+Fe), molar]. Shown are two types of bias behavior observed using a consistent analytical protocol for 6-µm diameter spot-size measurements. **(b)** Working calibration curves based on the data plotted in **(a)**, where bias values are normalized to end-member magnesite (expressed as $\delta^{13}C$ bias*(RM-UWMgs1)), which serves as the calibration anchor (crossed-circle denotes an outlier). Immediately below are the calibration residuals, which can be considered a measure of accuracy relative to the CRM NIST-19.

Fig. 6. The compositional dependence of certain base signals associated with SIMS $\delta^{13}C$ bias measurements from the magnesite-siderite series. **(a)** Secondary $^{12}C^-$ ion yields *vs.* Fe# and **(b)** the cumulative change in $\delta^{13}C_{raw}$ between the initial (*i*) and final (*f*) cycles of analysis ("$\Delta^{13}C(c_f - c_i)$") *vs.* Fe# under 6-µm spot-size analysis conditions. Yield = count rate (as mega-counts per second) / primary Cs^+ ion beam intensity (nA). Each point is an average of at least 4 measurements from 4 separate grains (1 analysis/grain). (See text for description of 'Type-I' *vs.* 'Type-II' bias trends).

Table 1. Source locality and measured extent of $\delta^{18}O$ and $\delta^{13}C$ homogeneity on the microanalytical scale of SIMS (10 and 6-µm scale, respectively) for the magnesite-siderite RMs of this study.

Table 2. Average chemical composition of the magnesite-siderite RMs of this study (analyzed by EPMA)

Table 3. SIMS $\delta^{18}O$ bias data for magnesite-siderite calibration RMs of this study, measured during multiple analytical sessions over a 2-year period (2015-2017).

Table 4. SIMS $\delta^{13}C$ bias data for magnesite- siderite calibration RMs of this study, measured during multiple analytical sessions over a 2-year period (2015-2017).

Table 5. Results of crystallographic orientation effect test on measured $\delta^{18}O$ bias.

Appendix A. Results of conventional phosphoric acid digestion and gas-source mass spectrometric analyses performed on the magnesite-siderite RMs of this study.

Supplemental Appendix 1. Supplementary electron microprobe analysis (EPMA) data table.

Supplemental Appendix 2. Complete SIMS datasets for all reported analytical sessions.

Supplemental Appendix 3. Graphical description of the influence of the curve-shape parameters *n, k,* and *d* on equation 6, along with additional examples of calibration curves and corresponding cycle-by-cycle data.

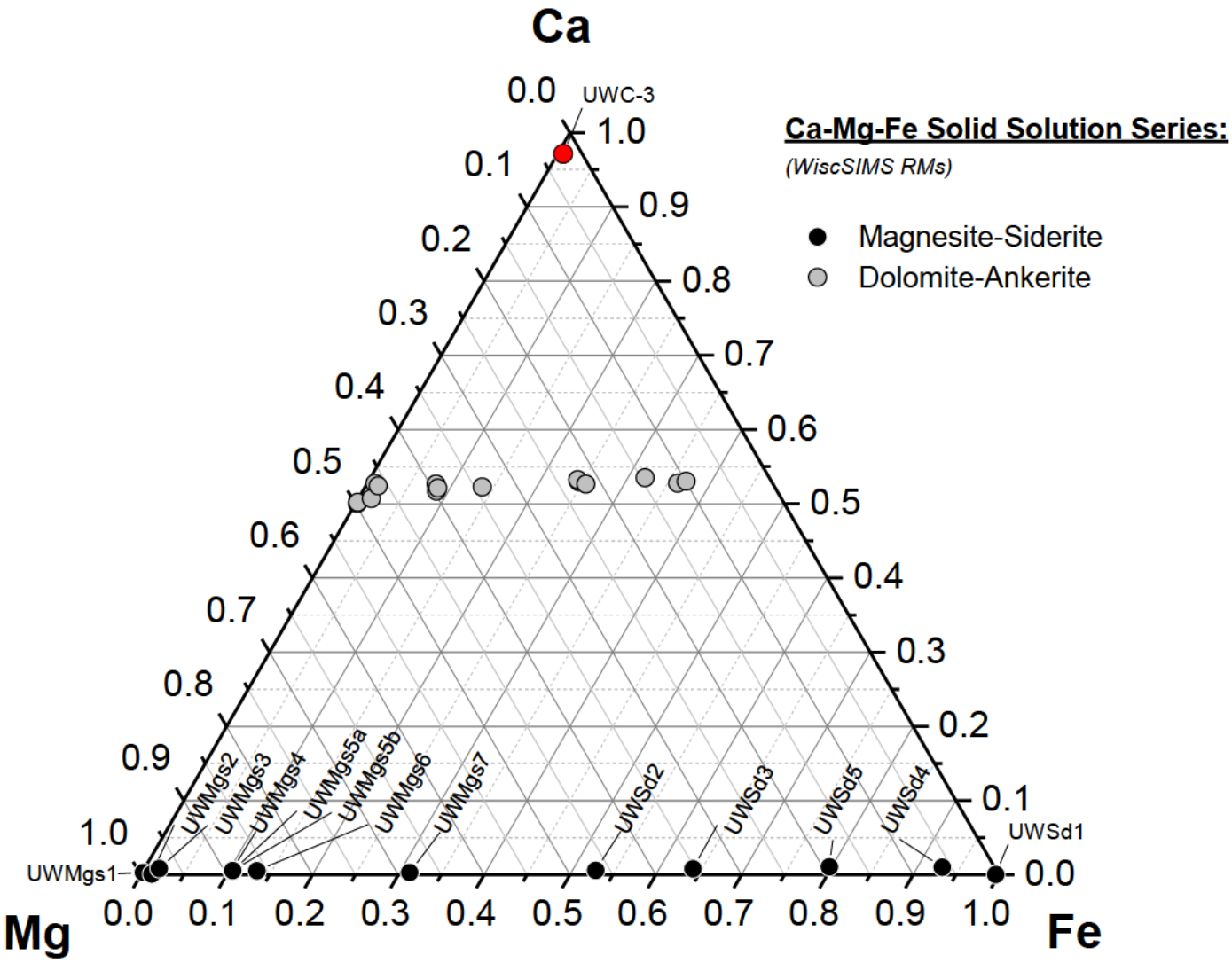
Ca
Mg
Fe
UWC-3
UWMgs1
UWSd1
UWMgs2
UWMgs3
UWMgs4
UWMgs5a
UWMgs5b
UWMgs6
UWMgs7
UWSd2
UWSd3
UWSd5
UWSd4
Ca-Mg-Fe Solid Solution Series:
(WiscSIMS RMs)
Magnesite-Siderite
Dolomite-Ankerite

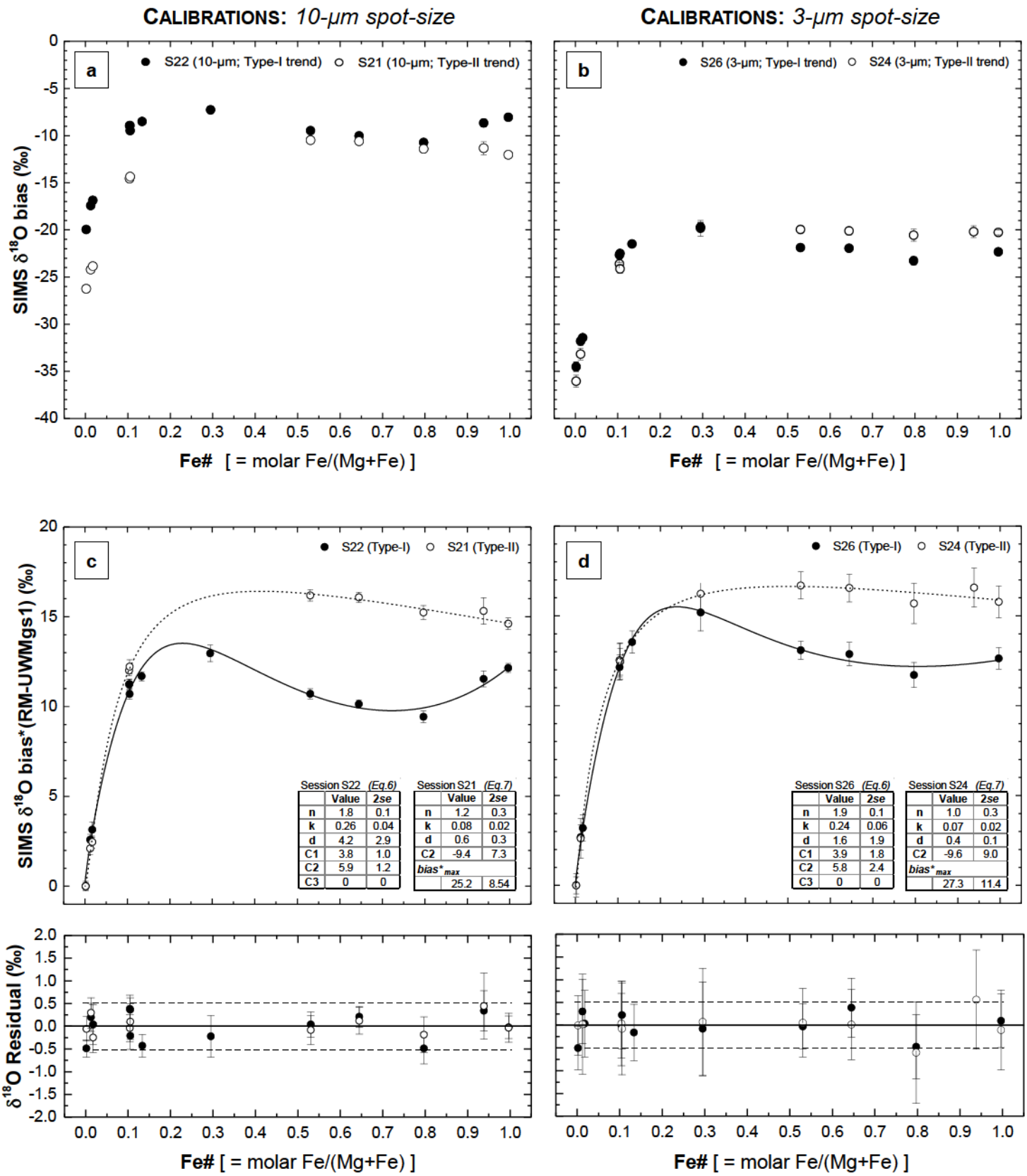
CALIBRATIONS: 10-µm spot-size
CALIBRATIONS: 3-µm spot-size
a
S22 (10-µm; Type-I trend)
S21 (10-µm; Type-II trend)
b
S26 (3-µm; Type-I trend)
S24 (3-µm; Type-II trend)
SIMS δ18O bias (‰)
Fe# [= molar Fe/(Mg+Fe)]
c
S22 (Type-I)
S21 (Type-II)
d
S26 (Type-I)
S24 (Type-II)
SIMS δ18O bias*(RM-UWMgs1) (‰)
Session S22 (Eq.6)
Value 2se
n 1.8 0.1
k 0.26 0.04
d 4.2 2.9
C1 3.8 1.0
C2 5.9 1.2
C3 0 0
Session S21 (Eq.7)
Value 2se
n 1.2 0.3
k 0.08 0.02
d 0.6 0.3
C2 -9.4 7.3
bias*max 25.2 8.54
Session S26 (Eq.6)
Value 2se
n 1.9 0.1
k 0.24 0.06
d 1.6 1.9
C1 3.9 1.8
C2 5.8 2.4
C3 0 0
Session S24 (Eq.7)
Value 2se
n 1.0 0.3
k 0.07 0.02
d 0.4 0.1
C2 -9.6 9.0
bias*max 27.3 11.4
δ18O Residual (‰)
Fe# [= molar Fe/(Mg+Fe)]

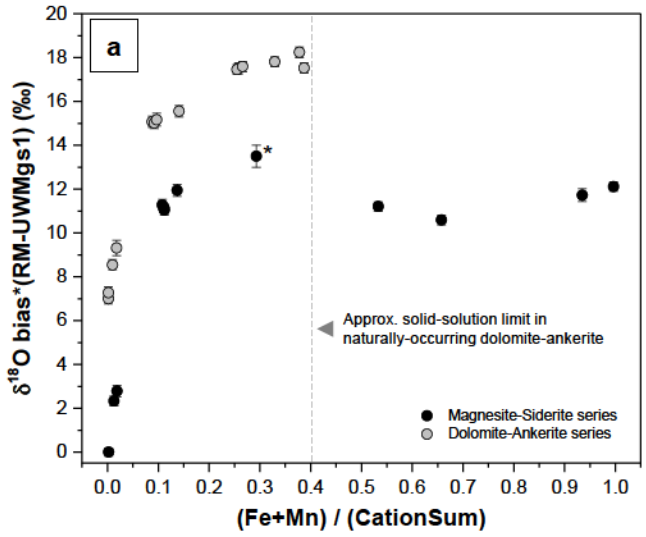
a
δ18O bias*(RM-UWMgs1) (‰)
(Fe+Mn) / (CationSum)
Approx. solid-solution limit in
naturally-occurring dolomite-ankerite
Magnesite-Siderite series
Dolomite-Ankerite series

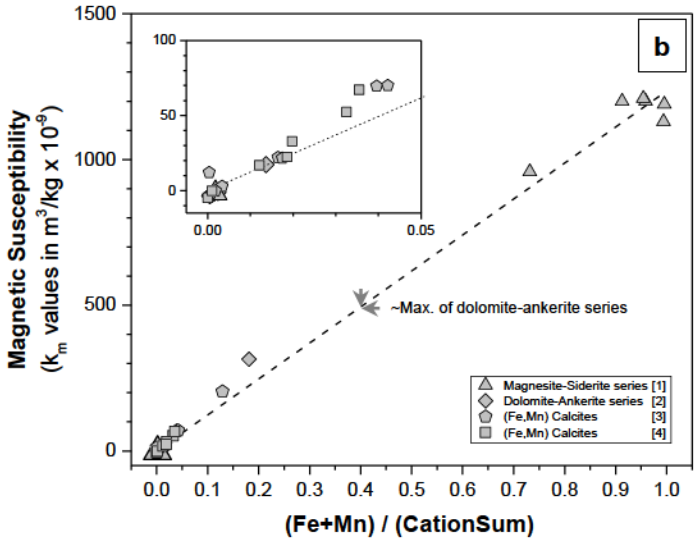
b
Magnetic Susceptibility
(km values in m3/kg x 10-9)
(Fe+Mn) / (CationSum)
~Max. of dolomite-ankerite series
Magnesite-Siderite series [1]
Dolomite-Ankerite series [2]
(Fe,Mn) Calcites [3]
(Fe,Mn) Calcites [4]

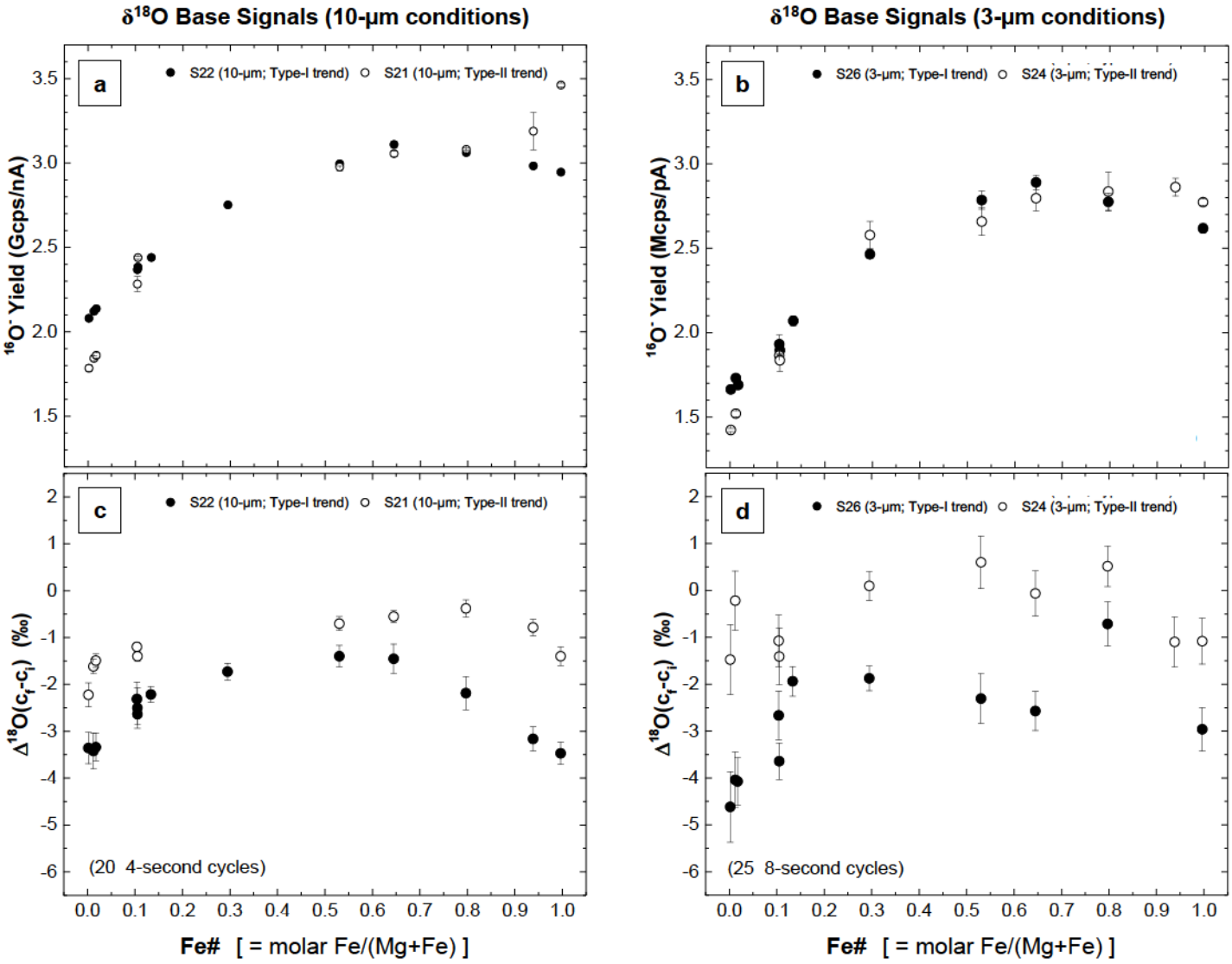
δ18O Base Signals (10-µm conditions)
δ18O Base Signals (3-µm conditions)
a
b
c
d
S22 (10-µm; Type-I trend)
S21 (10-µm; Type-II trend)
S26 (3-µm; Type-I trend)
S24 (3-µm; Type-II trend)
16O- Yield (Gcps/nA)
16O- Yield (Mcps/pA)
Δ18O(cf-ci) (‰)
(20 4-second cycles)
(25 8-second cycles)
Fe# [= molar Fe/(Mg+Fe)]

CALIBRATIONS: *6-μm spot-size*

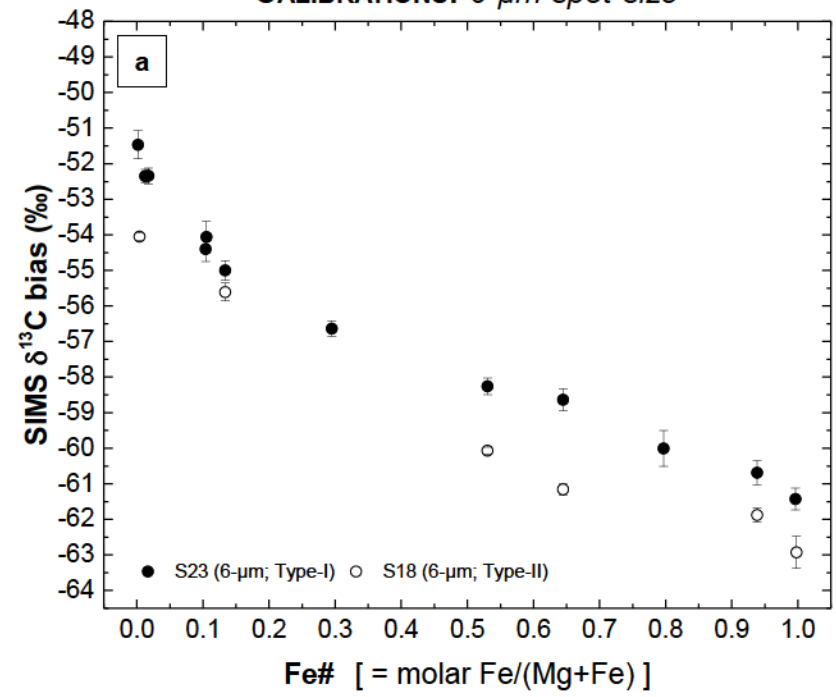

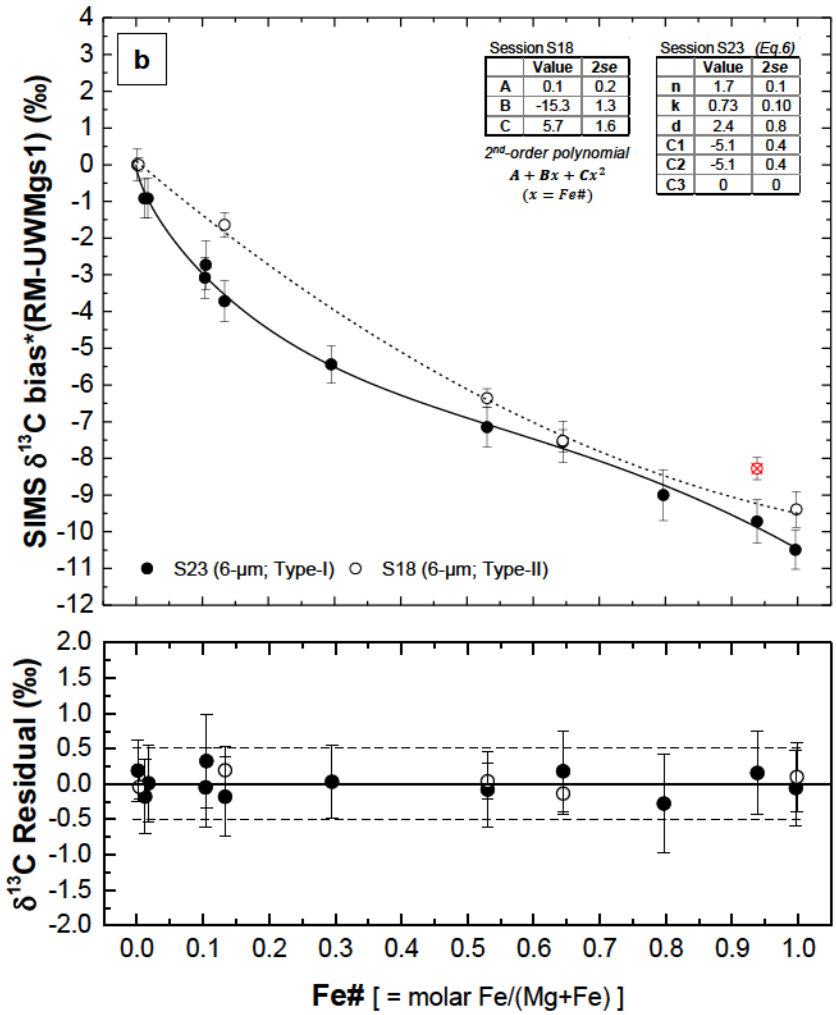

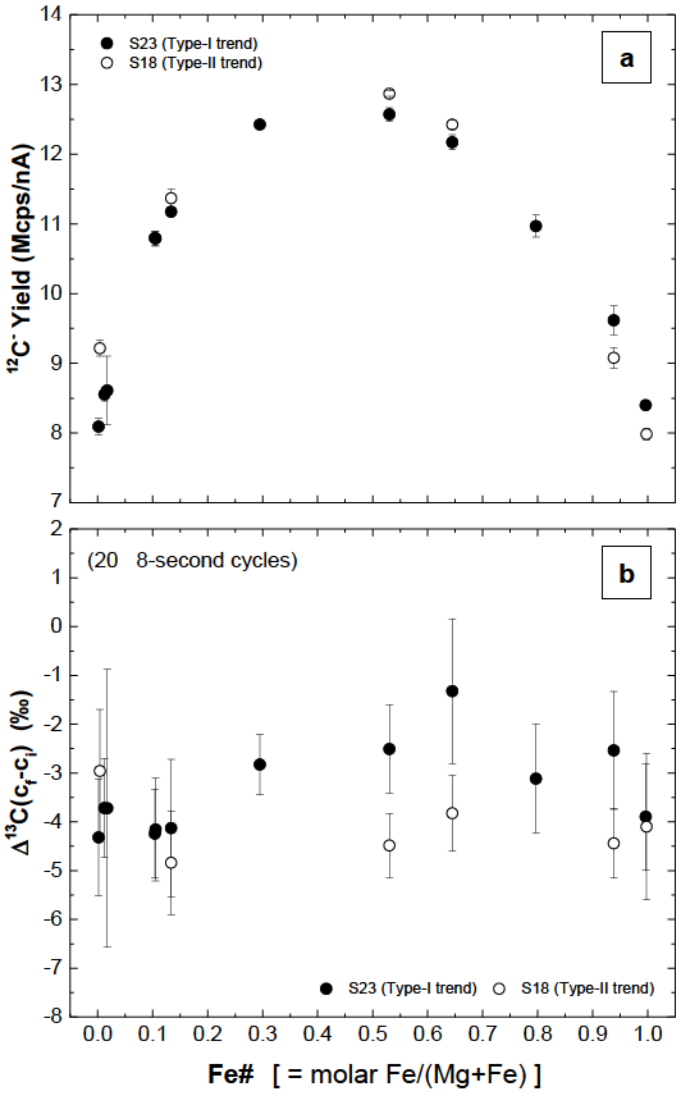
S23 (Type-I trend)
S18 (Type-II trend)
a
$^{12}C^-$ Yield (Mcps/nA)
(20 8-second cycles)
b
$\Delta^{13}C(c_f-c_i)$ (‰)
S23 (Type-I trend)
S18 (Type-II trend)
Fe# [= molar Fe/(Mg+Fe)]

Table 1. Source locality and measured extent of $\delta^{18}O$ and $\delta^{13}C$ homogeneity on the microanalytical scale of SIMS (10 and 6-µm scale, respectively) in the magnesite-siderite RMs of this study.

RM ID	Fe#	Source locality	True[a] $\delta^{18}O$ (‰, VSMOW)	True[a] $\delta^{13}C$ (‰, VPDB)	SIMS $\delta^{18}O$ homogeneity assessment					SIMS $\delta^{13}C$ homogeneity assessment				
					Session ID	*G*rains (*n*)	Analyses (*n*)	2*s*	2*se*	Session ID	*G*rains (*n*)	Analyses (*n*)	2*s*	2*se*
UWMgs1	0.002	Brumado District, Brazil	12.28	-0.82	S19	20	20	0.34	0.08	S20	20	20	0.84	0.19
UWMgs2	0.012	Italy (no additional details known)	16.99	-5.03	S19	19	20	0.46	0.10	S20	19	20	0.88	0.20
UWMgs3[b]	0.017	Steiermark, Austria (Oberdorf an der Laming?)	10.58	-0.32	S19	21	25	0.86	0.17	S20	20	20	0.99	0.22
UWMgs4	0.104	Gassetts, Chester, Windsor Co., Vermont, USA	12.62	-11.97	S19	19	20	0.32	0.07	S20	19	20	1.00	0.22
UWMgs5a[b]	0.105	Val di Vizze, Trentino-Alto Adige, Bolzano, Italy	11.01	-4.92	S19	19	20	0.44	0.10	S20	19	20	0.90	0.20
UWMgs5b[b]	0.105	Val di Vizze, Trentino-Alto Adige, Bolzano, Italy	11.01	-4.90	S19	20	20	0.36	0.08	-	-	-	-	-
UWMgs6[c]	0.134	Adige River (upper part of); Val di Vizze, Trentino-Alto Adige, Bolzano, Italy	10.94	-4.95	S16	15	23	0.69	0.14	S17	15	23	1.02	0.21
UWMgs7[d]	0.295	Savage River mine area, Tasmania, Australia	16.61	1.35	S22	22	23	1.89	0.39	S23	17	20	0.92	0.20
UWSd2	0.530	Morro Velho Mine, Nova Lima, Minas Gerais, Brazil	15.88	-4.03	S16	17	20	0.36	0.08	S18	17	20	0.46	0.10
UWSd3	0.645	Morro Velho Mine, Nova Lima, Minas Gerais, Brazil	15.30	-5.06	S16	17	20	0.25	0.06	S18	17	21	0.72	0.16
UWSd4[b]	0.938	Mount St. Hilaire, Quebec,	9.14	-5.49	S16	23	22	0.81	0.17	S18	20	20	0.85	0.19
UWSd5	0.797	Locality unknown	10.48	-7.28	S16	19	21	0.56	0.12	S20	18	19	0.90	0.21
UWSd1	0.997	Ivigtut Cryolite deposit, Ivittuut (Ivigtut), Arsuk Fjord, Sermersooq, Greenland	7.92	-8.07	S19	20	20	0.36	0.08	S20	20	20	0.59	0.13

[a] $\delta^{18}O$ and $\delta^{13}C$ VSMOW value determined by conventional phosphoric acid digestion and gas-source mass spectrometry (see Appendix A)

[b] Two separate splits of this material were evaluated.

[c] Denotes an RM which may be used for $\delta^{18}O$ calibration only if analyzed repeatedly a sufficient number of times to drive the standard error (at the 95% confidence leve) below 0.3‰ (approx. n = 8)

[d] This RM is not preferred for routine use in $\delta^{18}O$ calibration. Approx. 25+ replicate measurements are required to drive the standard error to approx. 0.3‰.

Table 2. Average chemical composition of the magnesite-siderite RMs of this study (analyzed by EPMA)

RM ID	Grains (*n*)	EPMA analyses (*n*)	%$MgCO_3$	2*s*	%$CaCO_3$	2*s*	%$FeCO_3$	2*s*	%$MnCO_3$	2*s*	%$SrCO_3$	2*s*	Fe# (Fe/(Mg+Fe))	2*s*	2*se*	Fe# (with Mn)	2*s*	2*se*	Fe (wt. %)	2*s*	2*se*
UWMgs1	20	60	99.47%	0.27%	0.29%	0.31%	0.17%	0.08%	0.07%	0.03%	<DL	-	0.002	0.001	0.000	0.002	0.001	0.000	0.11	0.05	0.01
UWMgs2	19	57	98.66%	0.47%	0.09%	0.08%	1.25%	0.42%	0.02%	0.02%	<DL	-	0.012	0.004	0.001	0.013	0.004	0.001	0.80	0.27	0.04
UWMgs3	21	63	97.29%	1.30%	0.84%	1.34%	1.73%	0.23%	0.14%	0.04%	<DL	-	0.017	0.002	0.000	0.019	0.002	0.000	1.11	0.15	0.02
UWMgs4	19	57	88.65%	0.35%	0.54%	0.11%	10.29%	0.34%	0.51%	0.09%	<DL	-	0.104	0.003	0.000	0.109	0.003	0.000	6.41	0.23	0.03
UWMgs5a[(a)]	21	61	88.26%	0.82%	0.55%	0.18%	10.39%	1.16%	0.80%	0.26%	<DL	-	0.105	0.011	0.001	0.113	0.009	0.001	6.46	0.72	0.09
UWMgs5b[(a)]	19	57	88.30%	0.72%	0.55%	0.20%	10.36%	1.05%	0.79%	0.23%	<DL	-	0.105	0.010	0.001	0.112	0.008	0.001	6.44	0.64	0.09
UWMgs6	15	46	85.76%	1.63%	0.52%	0.15%	13.22%	1.84%	0.50%	0.16%	<DL	-	0.134	0.018	0.003	0.138	0.017	0.003	8.13	1.10	0.16
UWMgs7	21	65	68.52%	1.32%	0.29%	0.18%	28.64%	1.11%	2.56%	0.37%	<DL	-	0.295	0.012	0.001	0.313	0.013	0.002	16.80	0.63	0.08
UWSd2	16	48	46.10%	0.84%	0.59%	0.39%	52.07%	0.96%	1.24%	0.17%	<DL	-	0.530	0.009	0.001	0.536	0.009	0.001	28.39	0.62	0.09
UWSd3	17	51	33.47%	2.07%	0.77%	0.18%	60.76%	2.29%	5.00%	0.33%	<DL	-	0.645	0.023	0.003	0.663	0.021	0.003	32.05	1.08	0.15
UWSd4	21	61	5.58%	1.36%	0.93%	1.03%	85.14%	3.89%	8.35%	2.27%	<DL	-	0.938	0.016	0.002	0.944	0.014	0.002	41.84	1.74	0.22
UWSd5	19	53	19.21%	2.35%	1.07%	0.49%	75.46%	1.85%	4.25%	1.65%	<DL	-	0.797	0.022	0.003	0.806	0.023	0.003	38.02	1.02	0.14
UWSd1	22	69	0.33%	0.10%	0.03%	0.02%	95.34%	0.29%	4.32%	0.24%	<DL	-	0.997	0.001	0.000	0.997	0.001	0.000	46.23	0.58	0.07

[(a)] Replicate splits

Table 3. SIMS $\delta^{18}O$ bias data for magnesite-siderite calibration RMs of this study, measured during multiple analytical sessions over a 2-year period (2015-2017).

Session ID	Spot size (µm)	Trend type	RM ID	Fe#[a]	$\delta^{18}O$ True[b] (‰, VSMOW)	$\delta^{18}O$ raw[c]	2se	$\delta^{18}O$ bias[c,d]	2se	$\delta^{18}O$ bias*(RM-UWMgs1)[e]	2se	$^{18}O^-$ Yield (Gcps/nA)	2se	$\Delta^{18}O(c_f\text{-}c_i)$[f]	2se
S16[g]	10	Type-I	Brazil Mgs[g,h]	0.004	15.01	-4.58	0.02	-19.30	0.02	0.00	0.10	1.791	0.014	-2.84	0.37
S16[g]	10	Type-I	UWMgs1	0.002	12.28	-	-	-	-	-	-	-	-	-	-
S16[g]	10	Type-I	UWMgs2	0.012	16.99	-	-	-	-	-	-	-	-	-	-
S16[g]	10	Type-I	UWMgs3	0.017	10.58	-	-	-	-	-	-	-	-	-	-
S16[g]	10	Type-I	UWMgs4	0.104	12.62	-	-	-	-	-	-	-	-	-	-
S16[g]	10	Type-I	UWMgs5a	0.105	11.01	-	-	-	-	-	-	-	-	-	-
S16[g]	10	Type-I	UWMgs5b	0.105	11.01	-	-	-	-	-	-	-	-	-	-
S16[g]	10	Type-I	UWMgs6	0.134	10.94	2.17	0.15	-8.68	0.15	11.38	0.19	2.195	0.016	-2.08	0.15
S16[g]	10	Type-I	UWMgs7	0.295	16.61							-	-	-	-
S16[g]	10	Type-I	UWSd2	0.530	15.88	6.27	0.08	-9.46	0.08	10.64	0.16	2.869	0.006	-1.11	0.15
S16[g]	10	Type-I	UWSd3	0.645	15.30	5.05	0.06	-10.09	0.06	10.00	0.15	3.009	0.008	-0.83	0.10
S16[g]	10	Type-I	UWSd4	0.938	9.14	0.18	0.17	-8.88	0.17	11.21	0.22	2.944	0.082	-2.13	0.21
S16[g]	10	Type-I	UWSd5	0.797	10.48	-0.40	0.12	-10.77	0.12	9.24	0.18	3.014	0.009	-1.30	0.23
S16[g]	10	Type-I	UWSd1	0.997	7.92	-	-	-	-	-	-	-	-	-	-
S16[g]	10	Type-I	Ivig. Sd[i]	0.998	7.79	-0.46	0.12	-8.18	0.12	11.33	0.16	2.960	0.008	-2.94	0.28
S19	10	Type-I	Brazil Mgs[h]	0.004	15.01	-	-	-	-	-	-	-	-	-	-
S19	10	Type-I	UWMgs1	0.002	12.28	-8.33	0.08	-20.36	0.08	0.00	0.19	1.826	0.006	-3.42	0.21
S19	10	Type-I	UWMgs2	0.012	16.99	-1.40	0.10	-18.14	0.10	2.33	0.22	1.874	0.007	-3.24	0.17
S19	10	Type-I	UWMgs3	0.017	10.58	-7.15	0.17	-17.64	0.17	2.78	0.26	1.870	0.007	-3.04	0.15
S19	10	Type-I	UWMgs4	0.104	12.62	3.21	0.07	-9.37	0.07	11.28	0.25	2.093	0.010	-2.42	0.17
S19	10	Type-I	UWMgs5a	0.105	11.01	1.46	0.10	-9.60	0.10	11.04	0.22	2.060	0.008	-2.50	0.21
S19	10	Type-I	UWMgs5b	0.105	11.01	1.76	0.08	-9.50	0.08	11.14	0.21	2.052	0.010	-2.24	0.18
S19	10	Type-I	UWMgs6	0.134	10.94	2.60	0.18	-8.71	0.18	11.94	0.28	2.172	0.013	-2.12	0.24
S19	10	Type-I	UWMgs7	0.295	16.61							-	-	-	-
S19	10	Type-I	UWSd2	0.530	15.88	6.56	0.04	-9.43	0.04	11.21	0.21	2.702	0.004	-1.02	0.37
S19	10	Type-I	UWSd3	0.645	15.30	5.36	0.09	-10.04	0.09	10.59	0.22	2.861	0.018	-0.79	0.29
S19	10	Type-I	UWSd4	0.938	9.14	0.38	0.20	-8.93	0.20	11.72	0.29	2.829	0.010	-3.06	0.21
S19	10	Type-I	UWSd5[j]	0.797	10.48	-	-	-	-	-	-	-	-	-	-
S19	10	Type-I	UWSd1[k]	0.997	7.92	-0.50	0.08	-8.55	0.08	12.11	0.22	2.767	0.005	-3.79	0.14
S19	10	Type-I	Ivig. Sd[i]	0.998	7.79	-	-	-	-	-	-	-	-	-	-
S21	10	Type-II	Brazil Mgs[h]	0.004	15.01	-	-	-	-	-	-	-	-	-	-
S21	10	Type-II	UWMgs1	0.002	12.28	-14.29	0.26	-26.25	0.26	0.00	0.27	1.784	0.019	-2.22	0.26
S21	10	Type-II	UWMgs2	0.012	16.99	-7.63	0.20	-24.21	0.20	2.10	0.33	1.843	0.014	-1.62	0.15
S21	10	Type-II	UWMgs3	0.017	10.58	-13.52	0.20	-23.85	0.20	2.46	0.33	1.860	0.015	-1.49	0.14
S21	10	Type-II	UWMgs4	0.104	12.62	-2.12	0.13	-14.56	0.13	12.01	0.30	2.283	0.045	-1.20	0.17
S21	10	Type-II	UWMgs5a	0.105	11.01	-3.86	0.26	-14.35	0.26	12.22	0.39	2.439	0.007	-1.00	0.18
S21	10	Type-II	UWMgs5b	0.105	11.01	-	-	-	-	-	-	-	-	-	-
S21	10	Type-II	UWMgs6	0.134	10.94	-	-	-	-	-	-	-	-	-	-
S21	10	Type-II	UWMgs7	0.295	16.61	-	-	-	-	-	-	-	-	-	-
S21	10	Type-II	UWSd2	0.530	15.88	4.83	0.15	-10.48	0.15	16.19	0.32	2.977	0.024	-0.70	0.15
S21	10	Type-II	UWSd3	0.645	15.30	4.14	0.07	-10.59	0.07	16.08	0.29	3.056	0.016	-0.55	0.12
S21	10	Type-II	UWSd4	0.938	9.14	-2.70	0.68	-11.33	0.68	15.32	0.73	3.189	0.110	-0.79	0.17
S21	10	Type-II	UWSd5[j]	0.797	10.48	-1.45	0.28	-11.41	0.28	15.24	0.39	3.080	0.012	-0.38	0.18
S21	10	Type-II	UWSd1[k]	0.997	7.92	-4.56	0.07	-12.03	0.07	14.61	0.32	3.462	0.012	-1.42	0.15
S21	10	Type-II	Ivig. Sd[i]	0.998	7.79	-	-	-	-	-	-	-	-	-	-
S22	10	Type-I	Brazil Mgs[h]	0.004	15.01	-	-	-	-	-	-	-	-	-	-
S22	10	Type-I	UWMgs1	0.002	12.28	-7.93	0.16	-19.96	0.16	0.00	0.19	2.080	0.008	-3.40	0.30
S22	10	Type-I	UWMgs2	0.012	16.99	-0.73	0.24	-17.42	0.24	2.59	0.31	2.121	0.013	-3.40	0.40
S22	10	Type-I	UWMgs3	0.017	10.58	-6.41	0.37	-16.87	0.37	3.15	0.44	2.137	0.010	-3.30	0.30
S22	10	Type-I	UWMgs4	0.104	12.62	3.62	0.08	-8.95	0.08	11.23	0.30	2.368	0.012	-2.30	0.40
S22	10	Type-I	UWMgs5a	0.105	11.01	1.50	0.21	-9.47	0.21	10.70	0.30	2.379	0.010	-2.60	0.20
S22	10	Type-I	UWMgs5b	0.105	11.01	2.06	0.14	-8.92	0.14	11.26	0.26	2.384	0.006	-2.50	0.40
S22	10	Type-I	UWMgs6	0.134	10.94	2.49	0.10	-8.50	0.10	11.69	0.25	2.440	0.009	-2.20	0.20
S22	10	Type-I	UWMgs7	0.295	16.61	9.14	0.37	-7.26	0.37	12.96	0.46	2.752	0.011	-1.70	0.20
S22	10	Type-I	UWSd2	0.530	15.88	6.41	0.15	-9.47	0.15	10.71	0.28	2.995	0.0130	-1.40	0.20
S22	10	Type-I	UWSd3	0.645	15.30	5.22	0.04	-10.02	0.04	10.14	0.23	3.110	0.020	-1.50	0.30
S22	10	Type-I	UWSd4	0.938	9.14	0.46	0.37	-8.65	0.37	11.54	0.44	2.983	0.013	-3.20	0.30
S22	10	Type-I	UWSd5[j]	0.797	10.48	-0.26	0.25	-10.72	0.25	9.43	0.34	3.062	0.015	-2.20	0.40
S22	10	Type-I	UWSd1[k]	0.997	7.92	-0.10	0.12	-8.05	0.12	12.15	0.25	2.946	0.006	-3.50	0.20
S22	10	Type-I	Ivig. Sd[i]	0.998	7.79	-	-	-	-	-	-	-	-	-	-
S24	3	Type-II	Brazil Mgs[h]	0.004	15.01	-	-	-	-	-	-	-	-	-	-
S24	3	Type-II	UWMgs1	0.002	12.28	-24.21	0.65	-36.05	0.65	0.00	0.65	1.423	0.010	-1.48	0.74
S24	3	Type-II	UWMgs2	0.012	16.99	-16.75	0.61	-33.18	0.61	2.61	1.10	1.520	0.017	-0.22	0.63
S24	3	Type-II	UWMgs3	0.017	10.58	-	-	-	-	-	-	-	-	-	-
S24	3	Type-II	UWMgs4	0.104	12.62	-11.29	0.15	-23.61	0.15	12.53	0.93	1.865	0.006	-1.08	0.55
S24	3	Type-II	UWMgs5a	0.105	11.01	-13.40	0.45	-24.14	0.45	12.47	1.01	1.836	0.065	-1.41	0.60
S24	3	Type-II	UWMgs5b	0.105	11.01	-	-	-	-	-	-	-		-	-
S24	3	Type-II	UWMgs6	0.134	10.94	-	-	-	-	-	-	-		-	-
S24	3	Type-II	UWMgs7	0.295	16.61	-3.55	0.83	-19.83	0.83	16.23	1.18	2.578	0.081	0.10	0.31
S24	3	Type-II	UWSd2	0.530	15.88	-4.40	0.38	-19.96	0.38	16.69	0.75	2.658	0.081	0.60	0.56
S24	3	Type-II	UWSd3	0.645	15.30	-5.10	0.42	-20.10	0.42	16.55	0.77	2.796	0.074	-0.06	0.48
S24	3	Type-II	UWSd4	0.938	9.14	-11.23	0.62	-20.19	0.62	16.57	1.09	2.862	0.053	-1.10	0.53
S24	3	Type-II	UWSd5[j]	0.797	10.48	-10.30	0.64	-20.56	0.64	15.69	1.12	2.836	0.115	0.52	0.43
S24	3	Type-II	UWSd1[k]	0.997	7.92	-12.51	0.25	-20.27	0.25	15.78	0.88	2.773	0.018	-1.08	0.49
S24	3	Type-II	Ivig. Sd[i]	0.998	7.79	-	-	-	-	-	-	-	-	-	-
S26	3	Type-I	Brazil Mgs[h]	0.004	15.01	-	-	-	-	-	-	-	-	-	-
S26	3	Type-I	UWMgs1	0.002	12.28	-22.66	0.48	-34.52	0.48	0.00	0.48	1.664	0.008	-4.62	0.75
S26	3	Type-I	UWMgs2	0.012	16.99	-15.35	0.43	-31.80	0.43	2.68	0.71	1.731	0.021	-4.04	0.59
S26	3	Type-I	UWMgs3	0.017	10.58	-21.19	0.29	-31.44	0.29	3.19	0.73	1.690	0.013	-4.07	0.50
S26	3	Type-I	UWMgs4	0.104	12.62	-10.32	0.43	-22.66	0.43	12.14	0.71	1.931	0.054	-2.67	0.52
S26	3	Type-I	UWMgs5a	0.105	11.01	-11.74	0.33	-22.50	0.33	12.45	0.75	1.895	0.030	-3.64	0.39
S26	3	Type-I	UWMgs5b	0.105	11.01	-	-	-	-	-	-	-	-	-	-
S26	3	Type-I	UWMgs6	0.134	10.94	-10.79	0.24	-21.49	0.24	13.54	0.62	2.070	0.028	-1.94	0.32
S26	3	Type-I	UWMgs7	0.295	16.61	-3.41	0.49	-19.70	0.49	15.19	1.03	2.465	0.026	-1.88	0.26
S26	3	Type-I	UWSd2	0.530	15.88	-6.35	0.13	-21.88	0.13	13.09	0.50	2.785	0.054	-2.31	0.53
S26	3	Type-I	UWSd3	0.645	15.30	-6.99	0.31	-21.95	0.31	12.87	0.65	2.890	0.043	-2.57	0.42
S26	3	Type-I	UWSd4	0.938	9.14	-	-	-	-	-	-	-	-	-	-
S26	3	Type-I	UWSd5[j]	0.797	10.48	-13.03	0.41	-23.27	0.41	11.71	0.70	2.775	0.051	-0.72	0.47
S26	3	Type-I	UWSd1[k]	0.997	7.92	-14.58	0.34	-22.33	0.34	12.63	0.59	2.618	0.027	-2.96	0.46
S26	3	Type-I	Ivig. Sd[i]	0.998	7.79	-	-	-	-	-	-	-	-	-	-

[a] Fe# = molar Fe/(Mg+Fe); the uncertainties that accompany this EPMA-derived parameter are tabulated in Table 2

[b] $\delta^{18}O$ VSMOW value determined by conventional phosphoric acid digestion and gas-source mass spectrometry (see Appendix A)

[c] Value corrected for instrumental drift relative to UWC-3 Reference Bracket.

[d] Value calculated via equations 1 and 3

[e] Value calculated via equation 4

[f] Cumulative change in $\delta^{18}O_{fw}$ between the initial and final cycle of analysis

[g] Calibration data from this session was normalized to the Brazil Mgs end-member rather than to UWMgs1, which was not yet developed at this stage.

[h] RM from Eiler et al. (1997). $\delta^{18}O$ VSMOW value recalcuated using phosphoric acid-fractionation factor of Rosenbaum and Sheppard (1986).

[i] RM from Eiler et al. (1997)

[j] The RM UWSd5 is a new split of JE-Mg-Sid of Eiler et al. (1997).

[k] The RM UWSd1 is a new split of Ivig. Sd (grains of new split are not rimmed by an FeO coating).

Table 4. SIMS $\delta^{13}C$ bias data for magnesite-siderite calibration RMs of this study, measured during multiple analytical sessions over a 2-year period (2015-2017).

Session ID	Spot size (µm)	Trend type	RM ID	Fe#[a]	$\delta^{13}C$ True[b] (‰, VPDB)	$\delta^{13}C$ raw[(c)]	2se	$\delta^{13}C$ bias[(c,d)]	2se	$\delta^{13}C$ bias*(RM-UWMgs1)[(e)]	2se	$^{12}C^-$ Yield (Mcps/nA)	2se	$\Delta^{13}C(c_f\text{-}c_i)^{(f)}$	2se
S17	6	Type-II	Brazil Mgs[(g,h)]	0.004	-0.96	-54.71	0.06	-53.80	0.06	0.00	0.34	7.846	0.030	-3.17	1.30
S17	6	Type-II	UWMgs1	0.002	-0.82	-	-	-	-	-	-	-	-	-	-
S17	6	Type-II	UWMgs2	0.012	-5.03	-	-	-	-	-	-	-	-	-	-
S17	6	Type-II	UWMgs3	0.017	-0.32	-	-	-	-	-	-	-	-	-	-
S17	6	Type-II	UWMgs4	0.104	-11.97	-	-	-	-	-	-	-	-	-	-
S17	6	Type-II	UWMgs5a	0.105	-4.92	-	-	-	-	-	-	-	-	-	-
S17	6	Type-II	UWMgs5b	0.105	-4.90	-	-	-	-	-	-	-	-	-	-
S17	6	Type-II	UWMgs6	0.134	-4.95	-61.64	0.21	-55.90	0.21	-2.22	0.44	10.768	0.068	-3.82	0.85
S17	6	Type-II	UWMgs7	0.295	1.35	-	-	-	-	-	-	-	-	-	-
S17	6	Type-II	UWSd2	0.530	-4.03	-	-	-	-	-	-	-	-	-	-
S17	6	Type-II	UWSd3	0.645	-5.06	-66.59	0.20	-60.09	0.20	-6.65	0.59	11.497	0.051	-0.74	0.74
S17	6	Type-II	UWSd4	0.938	-5.49	-	-	-	-	-	-	-	-	-	-
S17	6	Type-II	UWSd5[(i)]	0.797	-7.28	-	-	-	-	-	-	-	-	-	-
S17	6	Type-II	UWSd1[(j)]	0.997	-8.07	-	-	-	-	-	-	-	-	-	-
S17	6	Type-II	Ivig. Sd[(k)]	0.998	-8.18	-70.90	0.29	-63.24	0.29	-9.97	0.45	8.086	0.056	-3.11	1.36
S18	6	Type-II	Brazil Mgs[(g,h)]	0.004	-0.96	-54.96	0.10	-54.05	0.10	0.00	0.18	9.216	0.114	-2.96	1.26
S18	6	Type-II	UWMgs1	0.002	-0.82	-	-	-	-	-	-	-	-	-	-
S18	6	Type-II	UWMgs2	0.012	-5.03	-	-	-	-	-	-	-	-	-	-
S18	6	Type-II	UWMgs3	0.017	-0.32	-	-	-	-	-	-	-	-	-	-
S18	6	Type-II	UWMgs4	0.104	-11.97	-	-	-	-	-	-	-	-	-	-
S18	6	Type-II	UWMgs5a	0.105	-4.92	-	-	-	-	-	-	-	-	-	-
S18	6	Type-II	UWMgs5b	0.105	-4.90	-	-	-	-	-	-	-	-	-	-
S18	6	Type-II	UWMgs6	0.134	-4.95	-60.72	0.25	-55.61	0.25	-1.64	0.34	11.368	0.128	-4.84	1.06
S18	6	Type-II	UWMgs7	0.295	1.35	-	-	-	-	-	-	-	-	-	-
S18	6	Type-II	UWSd2	0.530	-4.03	-64.21	0.10	-60.07	0.10	-6.36	0.26	12.867	0.040	-4.49	0.66
S18	6	Type-II	UWSd3	0.645	-5.06	-66.32	0.16	-61.16	0.16	-7.52	0.30	12.424	0.064	-3.82	0.77
S18	6	Type-II	UWSd4	0.938	-5.49	-67.10	0.19	-61.88	0.19	-8.28	0.30	9.077	0.147	-4.44	0.71
S18	6	Type-II	UWSd5[(i)]	0.797	-7.28	-	-	-	-	-	-	-	-	-	-
S18	6	Type-II	UWSd1[(j)]	0.997	-8.07	-	-	-	-	-	-	-	-	-	-
S18	6	Type-II	Ivig. Sd[(k)]	0.998	-8.18	-70.60	0.45	-62.93	0.45	-9.39	0.49	7.984	0.078	-4.10	1.50
S20	6	Type-I	Brazil Mgs[(n)]	0.004	-0.96	-	-	-	-	-	-	-	-	-	-
S20	6	Type-I	UWMgs1	0.002	-0.82	-50.77	0.19	-49.99	0.19	0.00	0.27	7.311	0.029	-2.63	0.84
S20	6	Type-I	UWMgs2	0.012	-5.03	-55.71	0.20	-50.26	0.20	-0.28	0.35	7.565	0.062	-2.85	0.60
S20	6	Type-I	UWMgs3	0.017	-0.32	-51.03	0.22	-50.46	0.22	-0.49	0.39	8.508	0.581	-2.95	0.56
S20	6	Type-I	UWMgs4	0.104	-11.97	-64.42	0.22	-52.59	0.22	-2.74	0.37	9.464	0.063	-3.21	0.89
S20	6	Type-I	UWMgs5a	0.105	-4.92	-57.74	0.20	-52.45	0.20	-2.59	0.39	9.531	0.057	-3.42	0.83
S20	6	Type-I	UWMgs5b	0.105	-4.90	-	-	-	-	-	-	-	-	-	-
S20	6	Type-I	UWMgs6	0.134	-4.95	-58.58	0.46	-52.65	0.46	-2.80	0.58	10.331	0.040	-3.75	1.23
S20	6	Type-I	UWMgs7	0.295	1.35	-	-	-	-	-	-	-	-	-	-
S20	6	Type-I	UWSd2	0.530	-4.03	-60.62	0.53	-56.40	0.53	-6.74	0.62	11.341	0.132	-1.74	1.11
S20	6	Type-I	UWSd3	0.645	-5.06	-62.57	0.36	-57.38	0.36	-7.78	0.48	10.974	0.077	-0.90	1.16
S20	6	Type-I	UWSd4	0.938	-5.49	-63.88	0.27	-58.29	0.27	-8.73	0.43	9.224	0.338	-2.05	1.47
S20	6	Type-I	UWSd5[(i)]	0.797	-7.28	-65.14	0.21	-58.06	0.21	-8.49	0.37	10.215	0.091	-0.88	1.17
S20	6	Type-I	UWSd1[(j)]	0.997	-8.07	-67.99	0.13	-59.80	0.13	-10.33	0.35	8.264	0.020	-3.72	1.00
S20	6	Type-I	Ivig. Sd[(k)]	0.998	-8.18	-	-	-	-	-	-	-	-	-	-
S23	6	Type-I	Brazil Mgs[(n)]	0.004	-0.96	-	-	-	-	-	-	-	-	-	-
S23	6	Type-I	UWMgs1	0.002	-0.82	-52.25	0.40	-51.47	0.40	0.00	0.43	8.092	0.118	-4.32	1.19
S23	6	Type-I	UWMgs2	0.012	-5.03	-57.18	0.19	-52.35	0.19	-0.92	0.53	8.554	0.095	-3.72	1.02
S23	6	Type-I	UWMgs3	0.017	-0.32	-52.71	0.22	-52.34	0.22	-0.92	0.54	8.610	0.493	-3.72	2.84
S23	6	Type-I	UWMgs4	0.104	-11.97	-65.72	0.35	-54.40	0.35	-3.08	0.56	10.796	0.101	-4.24	0.91
S23	6	Type-I	UWMgs5a	0.105	-4.92	-58.78	0.44	-54.06	0.44	-2.73	0.66	10.791	0.108	-4.16	1.05
S23	6	Type-I	UWMgs5b	0.105	-4.90	-	-	-	-	-	-	-	-	-	-
S23	6	Type-I	UWMgs6	0.134	-4.95	-59.74	0.28	-55.00	0.28	-3.72	0.56	11.174	0.012	-4.13	1.41
S23	6	Type-I	UWMgs7	0.295	1.35	-54.90	0.21	-56.64	0.21	-5.44	0.51	12.425	0.057	-2.83	0.62
S23	6	Type-I	UWSd2	0.530	-4.03	-62.22	0.23	-58.26	0.23	-7.15	0.53	12.570	0.096	-2.51	0.91
S23	6	Type-I	UWSd3	0.645	-5.06	-63.57	0.31	-58.64	0.31	-7.55	0.57	12.170	0.107	-1.32	1.49
S23	6	Type-I	UWSd4	0.938	-5.49	-65.91	0.34	-60.69	0.34	-9.72	0.59	9.617	0.206	-2.54	1.21
S23	6	Type-I	UWSd5[(i)]	0.797	-7.28	-67.02	0.50	-60.01	0.50	-9.00	0.69	10.968	0.157	-3.12	1.12
S23	6	Type-I	UWSd1[(j)]	0.997	-8.07	-69.00	0.31	-61.43	0.31	-10.49	0.53	8.399	0.038	-3.90	1.09
S23	6	Type-I	Ivig. Sd[(k)]	0.998	-8.18	-	-	-	-	-	-	-	-	-	-

[a] Fe# = molar Fe/(Mg+Fe); the uncertainties that accompany this EPMA-derived parameter are tabulated in Table 2

[b] $\delta^{13}C$ VPDB value determined by conventional phosphoric acid digestion and gas-source mass spectrometry (see Appendix A)

[c] Value corrected for instrumental drift relative to UWC-3 Reference Bracket.

[d] Value calculated via equations 2 and 3

[e] Value calculated via equation 4

[f] Cumulative change in $\delta^{13}C_{raw}$ between the initial and final cycle of analysis

[g] Calibration data from this session was normalized to the Brazil Mgs end-member rather than to UWMgs1, which was not yet developed at this stage.

[h] RM from Eiler et al. (1997).

[i] The RM UWSd5 is a new split of JE-Mg-Sid of Eiler et al. (1997).

[j] The RM UWSd1 is a new split of Ivig. Sd (grains of new split are not rimmed by an FeO coating).

[k] RM from Eiler et al. (1997)

Table 5. Results of crystallographic orientation effect test on measured $\delta^{18}O$ bias.

RM ID	Fe#	Grain mount type	$\delta^{18}O_{raw}$ (‰)	$\delta^{18}O$ bias	$2s$ [(c)]	n
UWSd1	0.997	Regular[(a)]	-4.56	-12.38	0.26	4
UWSd1	0.997	Oriented[(b)]	-4.67	-12.49	0.28	8
UWMgs5a	0.105	Regular[(a)]	-3.86	-14.71	0.58	5
UWMgs5a	0.105	Oriented[(b)]	-3.90	-14.75	0.72	10
UWMgs4	0.104	Regular[(a)]	-2.12	-14.56	0.25	4
UWMgs4	0.104	Oriented[(b)]	-2.13	-14.57	0.29	8

[(a)] When grains are laid out on a flat casting plate, the rhombic geometry of carboante grains results in an under-representation of edges and apices.

[(b)] Mount with grain edges and apices oriented perpendicular to casting plate surface (grains embedded into deep grooves cuts into 1-mm thick and stiff carbon tape).

[(c)] Among-grain variability

Appendix A. Results of conventional phosphoric acid digestion and gas-source mass spectrometric analyses performed on the magnesite-siderite RMs of this study.

RM ID	Analysis i.d.	$\delta^{18}O$ (‰) Raw[a]	Acid-frac. factor (α)[b]	Temp. (°C)[c]	$\delta^{18}O$ (‰)[d] (VSMOW)	$\delta^{18}O$ (‰)[e] (VPDB)	$\delta^{13}C$ (‰)[e] (VPDB)
UWMgs1							
	C4-251-9	21.71	1.009331	100	12.26	-18.09	-0.82
	C4-251-11	21.74	1.009331	100	12.29	-18.06	-0.82
	C4-251-10	21.74	1.009331	100	12.29	-18.06	-0.81
	Average of 3 separate digestions (~5-mg each):				**12.28**	**-18.07**	**-0.82**
				2s	**0.03**	**0.03**	**0.01**
UWMgs2							
	C4-251-14	26.45	1.00933	100	16.97	-13.52	-5.02
	C4-251-13	26.50	1.00933	100	17.01	-13.48	-5.03
	C4-251-15	26.46	1.00933	100	16.98	-13.51	-5.03
	Average of 3 separate digestions (~5-mg each):				**16.99**	**-13.50**	**-5.03**
				2s	**0.05**	**0.05**	**0.01**
UWMgs3							
	C4-251-1	20.02	1.00932	100	10.60	-19.70	-0.33
	C4-251-2	20.00	1.00932	100	10.58	-19.72	-0.31
	C4-251-3	19.99	1.00932	100	10.57	-19.73	-0.31
	Average of 3 separate digestions (~5-mg each):				**10.58**	**-19.72**	**-0.32**
				2s	**0.03**	**0.03**	**0.02**
UWMgs4							
	C4-251-5	22.00	1.00928	100	12.61	-17.75	-11.98
	C4-251-6	22.03	1.00928	100	12.64	-17.72	-11.96
	Average of 3 separate digestions (~5-mg each):				**12.62**	**-17.74**	**-11.97**
				2s	**0.04**	**0.04**	**0.03**
UWMgs5a							
	C4-251-21	20.37	1.00928	100	10.99	-19.32	-4.92
	C4-251-22	20.39	1.00928	100	11.01	-19.30	-4.91
	C4-251-23	20.42	1.00928	100	11.04	-19.27	-4.92
	Average of 3 separate digestions (~5-mg each):				**11.01**	**-19.30**	**-4.92**
				2s	**0.05**	**0.05**	**0.01**
UWMgs5b							
	C4-251-17	20.34	1.00928	100	10.96	-19.35	-4.90
	C4-251-19	20.44	1.00928	100	11.06	-19.25	-4.90
	Average of 3 separate digestions (~5-mg each):				**11.01**	**-19.30**	**-4.90**
				2s	**0.14**	**0.14**	**0.00**
UWMgs6							
	C4-247-13	20.29	1.00926	100	10.93	-19.38	-4.96
	C4-248-2	20.29	1.00926	100	10.93	-19.38	-4.96
	C4-248-3	20.32	1.00926	100	10.96	-19.35	-4.96
	Average of 3 separate digestions (~5-mg each):				**10.94**	**-19.37**	**-4.95**
				2s	**0.03**	**0.03**	**0.01**
UWMgs7							
	C4-255-13	25.95	1.00918	100	16.62	-13.86	1.36
	C4-255-15	25.96	1.00918	100	16.63	-13.85	1.34
	C4-255-16	25.90	1.00918	100	16.57	-13.91	1.36
	Average of 3 separate digestions (~5-mg each):				**16.61**	**-13.87**	**1.35**
				2s	**0.06**	**0.06**	**0.02**
UWSd2							
	C4-247-11	25.06	1.00905	100	15.86	-14.60	-4.03
	C4-247-10	25.02	1.00905	100	15.82	-14.63	-4.04
	C4-248-1	25.14	1.00905	100	15.94	-14.52	-4.01
	Average of 3 separate digestions (~5-mg each):				**15.88**	**-14.58**	**-4.03**
				2s	**0.12**	**0.12**	**0.03**
UWSd3							
	Calculated with renormalized Ca-Mg-Fe; Mn excluded						
	C4-247-7	24.43	1.00899	100	15.30	-15.14	-5.06
	C4-247-6	24.47	1.00899	100	15.34	-15.10	-5.04
	C4-247-5	24.40	1.00899	100	15.27	-15.17	-5.07
	Average of 3 separate digestions (~5-mg each):				**15.30**	**-15.14**	**-5.06**
				2s	**0.07**	**0.07**	**0.03**
UWSd3[f]							
	Calculated as (Ca+Mn)-Mg-Fe						
	C4-247-7	24.43	1.00899	100	15.30	-15.14	-5.06
	C4-247-6	24.47	1.00899	100	15.34	-15.10	-5.04
	C4-247-5	24.40	1.00899	100	15.27	-15.17	-5.07
	Average of 3 separate digestions (~5-mg each):				**15.30**	**-15.14**	**-5.06**
				2s	**0.07**	**0.07**	**0.03**
UWSd4							
	C4-247-2	18.07	1.00884	100	9.15	-21.10	-5.50
	C4-247-1	18.06	1.00884	100	9.14	-21.11	-5.47
	Average of 3 separate digestions (~5-mg each):				**9.14**	**-21.11**	**-5.49**
				2s	**0.01**	**0.01**	**0.04**
UWSd1							
	C4-252-1	16.84	1.00881	100	7.96	-22.26	-8.08
	C4-252-2	16.78	1.00881	100	7.90	-22.32	-8.08
	C4-252-3	16.78	1.00881	100	7.90	-22.32	-8.06
	Average of 3 separate digestions (~5-mg each):				**7.92**	**-22.30**	**-8.07**
				2s	**0.07**	**0.07**	**0.02**
UWSd5							
	C4-252-9	19.49	1.00891	100	10.49	-19.80	-7.27
	C4-252-10	19.47	1.00891	100	10.47	-19.82	-7.28
	C4-252-11	19.48	1.00891	100	10.48	-19.81	-7.28
	Average of 3 separate digestions (~5-mg each):				**10.48**	**-19.81**	**-7.28**
				2s	**0.02**	**0.02**	**0.01**

[a] Value measured by gas-source mass spectrometery; raw $\delta^{18}O$ value prior to correction for phosphoric acid fractionation during carbonate digestion

[b] Phosphoric acid-fractionation factor for $\delta^{18}O$ (at 100°C) calculated using Equation 4 of Rosenbaum and Sheppard (1986) and the cation composition (Ca-Mg-Fe normalized) of each RM.

[c] Carbonate phosphoric acid digestion temperature (>4 hours)

[d] The RM "UWC-3" was analyzed concurrently as a quality control measure (calibrated to NIST-19: $\delta^{18}O$ = 12.49 ± 0.06 (2±), $\delta^{13}C$ = -0.91 ± 0.08 (2±); see Kozdon et al., 2009) . 15 replicate measurements yielded an average $\delta^{18}O$ value of 12.67 ± 0.13 (2±) (‰, VSMOW) and an average $\delta^{13}C$ value of -0.93 ± 0.04 (2±) (‰, VPDB). The phosphoric acid-fractionation factor for $\delta^{18}O$ (at 100°C) was calculated after Kim et al. (2007).

[e] VSMOW to VPDB conversion after Coplen et al. (1983).

[f] The effect of the Mn cation on the phosphoric acid-fractionation factor for the Magnesite-Siderite series (calculated here after Rosenbaum and Sheppard, 1986) was approximated by examining Fig. 1 in Glig et al. 2003, which shows that the effect of Mn is most similar to that of Ca for calcite group minerals. Thus, for this alternate calculation, the Mn-content of this RM was added to the Ca-content. The cations were then normalized to (Ca+Mn)-Mg-Fe and the acid-fractionation factor was calculated using Equation 4 of Rosenbaum and Sheppard (1986).